Mountain Wave Analysis Using Fourier Methods

John R. Roadcap

Final Report

1 October 2007

AIR FORCE RESEARCH LABORATORY
AIR FORCE MATERIEL COMMAND
Space Vehicles Directorate
29 Randolph Rd.
Hanscom AFB, MA 01731-3010

AFRL-RV-HA-TR-2007-1112

This technical report has been reviewed and is approved for publication.

/ signed /
Robert A. Morris, Chief
Battlespace Environment Division

/ signed /   / signed /
John R. Roadcap   Paul Tracy, Acting Chief
Battlespace Surveillance Innovation Center   Battlespace Surveillance Innovation Center

REPORT DOCUMENTATION PAGE		*Form Approved* *OMB No. 0704-01-0188*

The public reporting burden for this collection of information is estimated to average 1 hour per response, including the time for reviewing instructions, searching existing data sources, gathering and maintaining the data needed, and completing and reviewing the collection of information. Send comments regarding this burden estimate or any other aspect of this collection of information, including suggestions for reducing the burden to Department of Defense, Washington Headquarters Services Directorate for Information Operations and Reports (0704-0188), 1215 Jefferson Davis Highway, Suite 1204, Arlington VA 22202-4302. Respondents should be aware that notwithstanding any other provision of law, no person shall be subject to any penalty for failing to comply with a collection of information if it does not display a currently valid OMB control number.
PLEASE DO NOT RETURN YOUR FORM TO THE ABOVE ADDRESS.

1. REPORT DATE *(DD-MM-YYYY)* 30 Sep 2007	2. REPORT TYPE Scientific, Final	3. DATES COVERED *(From - To)*

4. TITLE AND SUBTITLE Mountain Wave Analysis Using Fourier Methods	5a. CONTRACT NUMBER
	5b. GRANT NUMBER
	5c. PROGRAM ELEMENT NUMBER 61102F
6. AUTHORS John R. Roadcap	5d. PROJECT NUMBER 2304
	5e. TASK NUMBER OT
	5f. WORK UNIT NUMBER A1

7. PERFORMING ORGANIZATION NAME(S) AND ADDRESS(ES) Air Force Research Laboratory /RVBYA 29 Randolph Road Hanscom AFB, MA 01731-3010	8. PERFORMING ORGANIZATION REPORT NUMBER AFRL-RV-HA-TR-2007-1112
9. SPONSORING/MONITORING AGENCY NAME(S) AND ADDRESS(ES)	10. SPONSOR/MONITOR'S ACRONYM(S) AFRL/RVBYA
	11. SPONSOR/MONITOR'S REPORT NUMBER(S)

12. DISTRIBUTION/AVAILABILITY STATEMENT
Approved for Public Release; distribution unlimited.

13. SUPPLEMENTARY NOTES

14. ABSTRACT

Eigenanalysis of temperature and wind profiles can reveal distinct resonances at mesoscale wavelengths. Fourier transform methods are well suited to analyze resonant modes such as mountain waves due, in part, to (1) their fast computation speed for large wave number domains compared to numerical forecast models and (2) their requirements for only a coarse horizontal background state. Common traits of Fourier mountain wave models include use of the Boussinesq approximation and neglect of moisture and Coriolis terms. Solutions are provided to linearized elliptic partial differential equations expressed in terms of height or velocity perturbation using complex phase functions. Lower boundary conditions are defined using the Fourier transform of the terrain height field which is typically modified to ensure linear assumptions are satisfied and to avoid effects associated with periodic horizontal boundary conditions. Two mountain wave models, Smith Three-Layer and Broutman MWFM-3, are examined. Both models have a strong theoretical basis and are well documented in the refereed literature. These models can allow for both hydrostatic and non-hydrostatic wavfe modes but do not permit more than one wind turning point in their representation of the phase functions. The two models have undergone limited verification for "real-world" environments using aircraft and satellite data and have been compared with non-linear numerical model integrations. The Broutman MWFM-3 model, having been developed to include tropospheric and stratospheric wave propagation and having no theoretical limit on top height, is favored for testing in an operational forecast environment.

15. SUBJECT TERMS

Mountain waves	Fourier transform	Gravity waves	Phase integral	Vertical dispersion
Airy function	Turning points	Caustics	Propagating and trapped wave modes	

16. SECURITY CLASSIFICATION OF:			17. LIMITATION OF ABSTRACT	18. NUMBER OF PAGES	19a. NAME OF RESPONSIBLE PERSON John Roadcap
a. REPORT	b. ABSTRACT	c. THIS PAGE			
UNCL	UNCL	UNCL	UNL	60	19B. TELEPHONE NUMBER *(Include area code)*

Contents

Figures

Tables

Acknowledgments

1. INTRODUCTION

Eigenanalysis of temperature and wind profiles often reveals distinct resonances at mesoscale horizontal wavelengths which are on the order of 2 km to 30 km. An example of such an analysis is described in Appendix A. These analyses suggest using linear methods that can identify and depict mesoscale resonant modes such as mountain waves. Fourier transform analysis methods, when properly posed, appear well-suited for this purpose.

The strengths of Fourier models apply to several areas. Gravity wave propagation methods using Fourier analysis can run faster on computers than mesoscale numerical prediction (NWP) models with comparable spatial resolution. This allows use of small computers in many applications. The linear assumptions inherent in Fourier analysis require only a horizontally-uniform background state which can be provided from relatively coarse numerical model output or rawinsonde data. The quasi-analytical solutions avoid numerical methods with their attendant error. Fourier methods use complex arithmetic which allows both modulus and phase information in the wave function. These methods also permit continuous functional behavior in the vertical.

Fourier methods used for mountain wave analysis also bear some resemblance to wave propagation methods employed in the physical sciences and engineering for determining wave dispersion and attenuation. This includes fields as distinct as oceanography, seismology, optics, and radio science.

There are notable limitations to Fourier analysis methods. A confined horizontal domain must typically be considered for analysis given the assumption of horizontally uniform background flow. Also, Fourier models cannot treat non-linear behavior, such as breaking waves, where small-amplitude wave perturbations interact with the larger scale uniform basic state. This inability to handle non-linear behavior may be its greatest limitation.

2. COMMON TRAITS OF FOURIER MOUNTAIN WAVE MODELS

Common traits of Fourier mountain wave models include the use of the Boussinesq approximation where the density is constant except for terms involving the external force (e.g. gravity) in the equations of motion (Chandrasekhar, 1961). The Boussinesq approximation allows no acoustic waves and permits only shallow oscillations relative to the atmospheric scale height. The anelastic approximation, which allows for deep motion, is sometimes used instead and typically results in the amplitude being scaled by the inverse square root of the density.

The Fourier models represent solutions to elliptic partial differential equations, expressed in terms of height or vertical velocity perturbation. These equations are derived from the governing system of three-dimensional (3-D) linearized partial differential equations for conservation of mass and momentum, and written in the complex wave number domain in the form:

$$\frac{\partial}{\partial z}(\sigma^2 \frac{\partial \hat{\eta}}{\partial z}) + (k_x^2 + k_y^2)(N^2 - \sigma^2)\hat{\eta} = 0 \quad (m\,s^{-2}\,rad)$$

Here $\hat{\eta}$ is the three-dimensional (3-D) complex height perturbation field, k_x and k_y are the horizontal wave numbers, N is the Brunt-Vaisala frequency, z is the vertical coordinate, and σ is the intrinsic frequency. Coriolis acceleration is typically neglected for the characteristic time scales involved with mountain waves (~ 30 minutes) and a steady-state background atmosphere is assumed in accord with linear theory. The models are "dry" in that no moisture effects including latent heat release are accounted for in the equations. Very detailed terrain can be included in the two-dimensional lower boundary with its detail limited only by the horizontal grid spacing. However, in accord with the linear assumption, the maximum value for η at the lower boundary must be much less than the total model depth.

The specification of the three-dimensional vertical wave number or phase function relation in the mountain wave model is critical. Vertically-propagating locally-plane waves are assumed. For vertically propagating wave modes, a general solution of the elliptic equations can be posed as:

$$\hat{\eta}(k_x, k_y, z) = \hat{h}(k_x, k_y) \cdot \hat{g}(k_x, k_y, z)\exp\left[i\hat{\phi}(k_x, k_y, z)\right] \qquad (m^3/rad) \qquad (1)$$

where the complex phase function $\hat{\phi}$ is defined in integral form as

$$\hat{\phi}(k_x, k_y, z) \equiv -\int_0^z m(k_x, k_y, z)\,dz \qquad (rad) \qquad (2)$$

Here m is the vertical wave number or dispersion relation, $\hat{h}$ is the terrain lower boundary, $\hat{\eta}$ is the wave height perturbation at some altitude z, and $\hat{g}$ is a density- or altitude-dependent function related to the vertical wave flux. The complex variables used in this expression are formulated in the wave number or transform domain as represented by the hatted symbol ^, where $i = \sqrt{-1}$. Specific forms of the dispersion relation m and function $\hat{g}$ for each model will be discussed in more detail below.

Some general relations can be quantified for the inclusion of phase and amplitude modulation in the Fourier models relative to wave dispersion. The vertical wave number m or dispersion relation is expressed as

$$m = \left[(k_x^2 + k_y^2)(N^2 - \sigma^2)/\sigma^2\right]^{1/2} \qquad (rad\ m^{-1}) \qquad (3)$$

where N is the Brunt-Vaisala frequency and σ is the intrinsic frequency of a fluid parcel moving through a stationary wave field. The Brunt-Vaisala frequency is the square root of the product of the vertical potential temperature gradient $d\bar{\theta}/dz$ (static stability) and the ratio of acceleration due to gravity and potential temperature. Specifically,

$$N = \left[\frac{g}{\bar{\theta}} \frac{d\bar{\theta}}{dz} \right]^{\frac{1}{2}} \qquad \text{(rad s}^{-1}) \qquad (4)$$

The Brunt-Vaisala frequency N or its square N^2 is also referred to as "static stability". Here, the over bar $\bar{}$ denotes the basic state or horizontally-uniform background value. For two-dimensional horizontal wind flow, the intrinsic frequency is defined as

$$\sigma = -k_x \bar{U} - k_y \bar{V} \qquad \text{(s}^{-1}) \qquad (5)$$

where $\bar{U}$ and $\bar{V}$ are the west-to-east and south-to-north background wind speeds, respectively. For the dispersion relation used throughout this report, the wind curvature terms such as $\frac{1}{\bar{U}} \frac{\partial^2 \bar{U}}{\partial z}$ are ignored since $\bar{U}$ and $\bar{V}$ are considered to be slowly varying with height.

Certain relations between the wave dispersion and vertical wave propagation characteristics exist given homogeneous background atmospheric conditions over a propagation layer where the phase angle $\phi = -\int_0^z m\,dz$ for a vertically propagating wave. If $N^2 - \sigma^2 > 0$, then m is real, the solution is trigonometric, and the phase is modulated. If $N^2 - \sigma^2 \gg 0$, the wave solution is non-dispersive and vertically propagating and m is nearly independent of σ in the two-dimensional limit. If $N^2 = \sigma^2$, this is referred to as the turning point height or buoyancy frequency turning point which will result in the trapping of waves. The role of the turning point height will be discussed in more detail later in this report. If $N^2 - \sigma^2 < 0$, then m is imaginary, the solution is exponential, and reflection of wave energy occurs below the level. If $\sigma^2 = 0$, a singularity exists in Eq. (3) which will result in a "critical layer" where wave absorption will occur with strong attenuation above the level of analysis. (Smith, 2002)

3. EVALUATION OF THE TWO-DIMENSIONAL FOURIER TRANSFORM

The mountain wave model equations at a given height are solved in the horizontal two-dimensional Fourier transform domain for a function $f(x, y, z)$:

$$F(k_x, k_y, z) = \frac{1}{2\pi} \int_{-\infty}^{\infty} \int_{-\infty}^{\infty} f(x, y, z) \exp\left[i\left(k_x x + k_y y\right)\right] dx\,dy \qquad (6)$$

using the Cartesian coordinate system (x, y, z) where k_x and k_y are horizontal wave numbers in x (west-to-east) and y (south-to-north) directions, respectively. Working in the complex transform domain allows for both modulus and phase information in the solution. These solutions are recovered for the spatial (and real) domain using the inverse Fourier transform.

In the numerical evaluation of the double Fourier transform such as Eq. (6), it is most efficient to express this function as two successive one-dimensional transforms. Following Sneddon (1951),

$$F(k_x, k_y) = \frac{1}{2\pi} \int_{-\infty}^{\infty} \int_{-\infty}^{\infty} f(x,y) e^{ik_x x} e^{ik_y y} \, dx \, dy$$

$$= \frac{1}{\sqrt{2\pi}} \int_{-\infty}^{\infty} \left[\frac{1}{\sqrt{2\pi}} \int_{-\infty}^{\infty} f(x,y) e^{ik_x x} dx \right] e^{ik_y y} dy$$

$$= \frac{1}{\sqrt{2\pi}} \int_{-\infty}^{\infty} \overline{f}(k_x, y) e^{ik_y y} dy = F(k_x, k_y)$$

This results in 2 n^3 operations per transform instead of n^4 operations when the integrand of Eq. (6) is treated as a four-dimensional function. Here n represents the number of functional data points to be transformed.

Further efficiency is obtained by using the fast Fourier transform (FFT) in lieu of the mathematical transform shown above. The fast Fourier transform is an algorithm specially designed for efficient machine calculation. The number of FFT operations for the one dimensional (1-D) Fourier transform is proportional to $n \log n$ rather than n^2 for the direct mathematical form. The one dimensional FFT algorithm listed in Brigham (1974) is used with the successive 1-D transform approach.

4. PRINCIPAL FOURIER MOUNTAIN WAVE MODELS

Two model approaches for Fourier mountain wave analysis have been considered. These include the Smith (Yale University) Fourier Three Layer model and the Broutman (Naval Research Laboratory) Mountain Wave Forecast Model.

The Smith-Yale Three-Layer model is based on a theoretical foundation that has been carefully developed since 1980. As its name implies, it uses a three layer profile of constant background velocity and static stability within a layer and, in general, does not permit wind turning with height. The model has been validated during field tests including the Mesoscale Alpine Program of 1999 (Smith et al, 2002).

The Broutman model, which is also known as the Mountain Wave Forecast Model version 3 (MWFM-3), uses continuous vertical profiles of wind shear and static stability. A transient or time-dependent solution is also available for trapped waves.

Both Fourier models were checked by their authors against numerical models integrated in time to a steady-state solution using the same basic state and lower boundary. The Smith-Yale model was checked against the COAMPS numerical model of the Naval Research Laboratory (NRL) and the MWFM-3 model was checked against the Lipps and Hemler (1982) model and the Weather Research and Forecasting (WRF) model. Some Fourier and numerical model comparisons are described briefly later in this report.

5. SMITH FOURIER THREE-LAYER MODEL

A two-dimensional Fourier transform for the general solution of the elliptic partial differential equation for vertical displacement η (in meters) is (following Smith, 2002)

$$\hat{\eta}(k,l,z) = A_i \exp(im_i z) + B_i \exp(-im_i z)$$

$$\hat{\eta} \equiv \frac{1}{2\pi} \int_{-\infty}^{\infty} \int_{-\infty}^{\infty} \eta(x,y,z) \exp\left[i\left(k_x x + k_y y\right)\right] dx\, dy \qquad \text{(m}^3\text{ rad}^{-1}) \qquad (7)$$

where the integers $i = 1, 2, 3$ denote three layers of constant wind velocity and stability, $A_i(k_x,k_y)$ and $B_i(k_x,k_y)$ are complex coefficients defined below, $m_i(k_x,k_y)$ is the complex dispersion relation or vertical wavenumber, and z is the height (in meters) above the model lower boundary. The vertical wavenumber m_i in a layer i for non-hydrostatic flow is expressed as

$$m_i^2 = \left(k_x^2 + k_y^2\right)\left(N_i^2 - \sigma_i^2\right)\big/\sigma_i^2 \qquad \text{(rad m}^{-2}) \qquad (8)$$

where $k_x = \dfrac{2\pi}{L_x}$, $k_y = \dfrac{2\pi}{L_y}$ (rad / m) are the horizontal wave numbers associated with the horizontal wavelengths L_x and L_y respectively, N_i is the layer Brunt-Vaisala frequency (rad sec^{-1}), and $\sigma_i = k_x U_i + k_y V_i$ is the layer intrinsic frequency. The intrinsic frequency σ is the frequency felt by a parcel of fluid moving through the stationary wave field. The vertical wave number and Fourier coefficients associated with a particular layer i will be selected according to the height or layer where z is defined.

The Fourier amplitude coefficients $A_i(k_x,k_y)$, $B_i(k_x,k_y)$ are computed using the transform of the terrain $\hat{h}(k_x,k_y)$ (m^3 radian^{-1}) and the dispersive parameters that define each layer (m_i,σ_i,z_i). The expressions for three layers in the Smith model are:

$$A_3 = \hat{h}/(FAE + q \cdot FBE)$$
$$A_1 = FAE \cdot A_3$$
$$B_1 = FBE \cdot A_3$$
$$A_2 = FCE \cdot A_3$$
$$B_2 = FDE \cdot A_3$$

where

$$FCE = (1/2)\left[1 + R_{32}\right]\exp\left(im_3 z_2 - im_2 z_2\right)$$
$$FDE = (1/2)\left[1 - R_{32}\right]\exp\left(im_3 z_2 + im_2 z_2\right)$$
$$FAE = (1/4)\left[\left(1 + R_{21}\right)\left(1 + R_{32}\right)\right]\exp\left(i(m_2 - m_1)z_1 + i\left(m_3 - m_2\right)z_2\right)$$
$$+ (1/4)\left[\left(1 - R_{21}\right)\left(1 - R_{32}\right)\right]\exp\left(-i(m_2 + m_1)z_1 + i\left(m_3 + m_2\right)z_2\right)$$
$$FBE = (1/4)\left[\left(1 - R_{21}\right)\left(1 + R_{32}\right)\right]\exp\left(i(m_2 + m_1)z_1 + i\left(m_3 - m_2\right)z_2\right)$$
$$+ (1/4)\left[\left(1 + R_{21}\right)\left(1 - R_{32}\right)\right]\exp\left(-i(m_2 - m_1)z_1 + i\left(m_3 + m_2\right)z_2\right)$$

and where

$$R_{32} = m_3 \sigma_3^2 / m_2 \sigma_2^2$$
$$R_{21} = m_2 \sigma_2^2 / m_1 \sigma_1^2$$

z_1 here is defined as the top of layer 1 and z_2 is the top of layer 2. All quantities are treated as complex. B_3 is set equal to zero for the top layer using the radiation condition at the upper boundary.

To give the model flexibility, a reflection coefficient q, different from unity, is introduced for the lower boundary to represent partial absorption of down-going waves. Dissipation of the wave by boundary layer turbulence or by critical layer absorption at the lower boundary can be parameterized by setting $q < 1$. When atmospheric conditions are uniform with height, then $R_{21} = R_{32} = 1$ and the down-going wave amplitudes are $B_1 = B_2 = 0$. The base level in the calculation is taken to be the reference height z_{ref} or the top of the pre-defined stagnant layer. The linearized lower boundary condition is then the height h of the terrain above the reference height z_{ref}:

$$\eta(x, y, 0) = h(x, y) - z_{ref} \tag{9}$$

Equation (7) is solved for $\hat{\eta}$ for any level z using the Fourier amplitude coefficients and dispersion relations that correspond to the layer where z is located. If z resides on a layer boundary, the coefficients in Eq. (7) are assigned for the layer below z. Diagnostic expressions for the perturbation vertical velocity amplitudes $\hat{w}$ and $\hat{u}$ are calculated in the Fourier domain using $\hat{\eta}$, the intrinsic frequency, and certain wave number relations. These velocity terms are expressed as:

$$\hat{w} = i\sigma\hat{\eta} \qquad\qquad \text{(m}^3\text{ s}^{-1}) \tag{10}$$

$$\hat{u} = \frac{k_x N \hat{w}}{\left(k_x^2 + k_y^2\right)^{1/2}\left(k_x U + k_y V\right)} \qquad\qquad \text{(m}^3\text{ s}^{-1}) \tag{11}$$

An inverse Fourier transform is then performed to display these variables in the real domain, in the form:

$$\eta(x, y, z) = \frac{1}{2\pi}\int_{-\infty}^{\infty}\int_{-\infty}^{\infty}\hat{\eta}(k_x, k_y, z)e^{-ik_x x}e^{-ik_y y}\,dk_x\,dk_y \qquad \text{(m)}$$

The perturbation temperature θ' at a given point can be calculated using η and the vertical gradient of mean potential temperature $\dfrac{\partial\bar{\theta}}{\partial z}$:

$$\theta' = \eta\frac{\partial\bar{\theta}}{\partial z} \qquad\qquad \text{(deg K)} \tag{12}$$

5.1   Computational Aspects of the Smith Three-Layer Model

Solutions at a given altitude are obtained for a 1024 x 1024 domain of horizontal grid points. This corresponds to a 2^p dimension using the base 2 FFT for $p = 10$. The

horizontal grid point spacing $\Delta x, \Delta y$ is 1 km resulting in a bandwidth or wave number differential $\Delta k_x = \Delta k_y = 2\pi/(n\Delta x) = 6.136 \times 10^{-6}$ rad/m.

For the terrain conditions, 30 arc-second terrain data from the NOAA GLOBE database (Hastings and Dunbar, 1998) are used to construct the lower terrain boundary height $h(x,y)$. The GLOBE database terrain heights are defined as a function of latitude and longitude, which corresponds to less than one km grid spacing for both latitudinal and longitudinal directions when it is mapped to a Cartesian grid. The latitudinal spacing is more or less constant with latitude while the longitudinal grid spacing decreases with increasing poleward latitude. For the model's purpose, the GLOBE terrain height data are interpolated to one km increments for the horizontal grid.

Equation (7) is evaluated at any wave number grid point at a given level except for those where critical levels or singularities occur in the dispersion relation (i.e., $\sigma = 0$). These grid points are skipped and are not included in the transform solution. Also, both a reference level and lower boundary reflection coefficient q must be defined. The reference level serves to reduce the lower model boundary terrain height by the height of the reference level above sea level. This reference level typically corresponds to the height of the boundary or "stagnant" layer. The lower boundary reflection coefficient appears in the expression for the 3rd layer coefficient $i = 3$ and is set to $q \leq 1$.

5.2 Practical Considerations

The terrain area $h(x,y)$ for the lower boundary condition is first padded by "zeroes" around its horizontal boundary for dimensional expansion of the computation domain necessary to meet numerical Fourier transform requirements. Typically, the expansion satisfies 2^p grid points in a single dimension for use in the FFT algorithm where p is an integer. The zero-padding, by definition, also minimizes truncation error of the discrete Fourier transform. However, truncation leads to a "wrap-around" effect, associated with periodic boundary conditions, where solutions occurring outside of the terrain area on one side of the computational domain will re-appear on the opposite side of the domain. For certain classes of terrain, an exponential decay with distance of terrain height from the high elevation point of the grid is introduced. This can smooth the joining of terrain boundaries and padding to minimize spurious waves introduced by discontinuities between the terrain and padded areas.

These terrain padding and transform operation procedures are illustrated in Figure 1. After subtracting the reference level from the terrain height, the terrain field is padded with zeroes to minimize "wrap-around" associated with periodic function truncation. If appropriate, an exponential decay of terrain height from the location of maximum height location may be introduced. This yields the field of $h(x,y)$ depicted at the top of Figure 1. The two-dimensional FFT of the $h(x,y)$ field yields the complex transform field

$H(k_x,k_y) = [H_r(k_x,k_y), H_i(k_x,k_y)]$, with H_r and H_i representing the real and imaginary

transform components respectively, which is depicted in the middle figure. This figure represents the operational wave number domain where the model solutions are obtained. The inverse transform of $H\left(k_x, k_y\right)$ yields (approximately) the original function $\bar{h}\left(x, y\right)$ which is shown at the bottom of Figure 1.
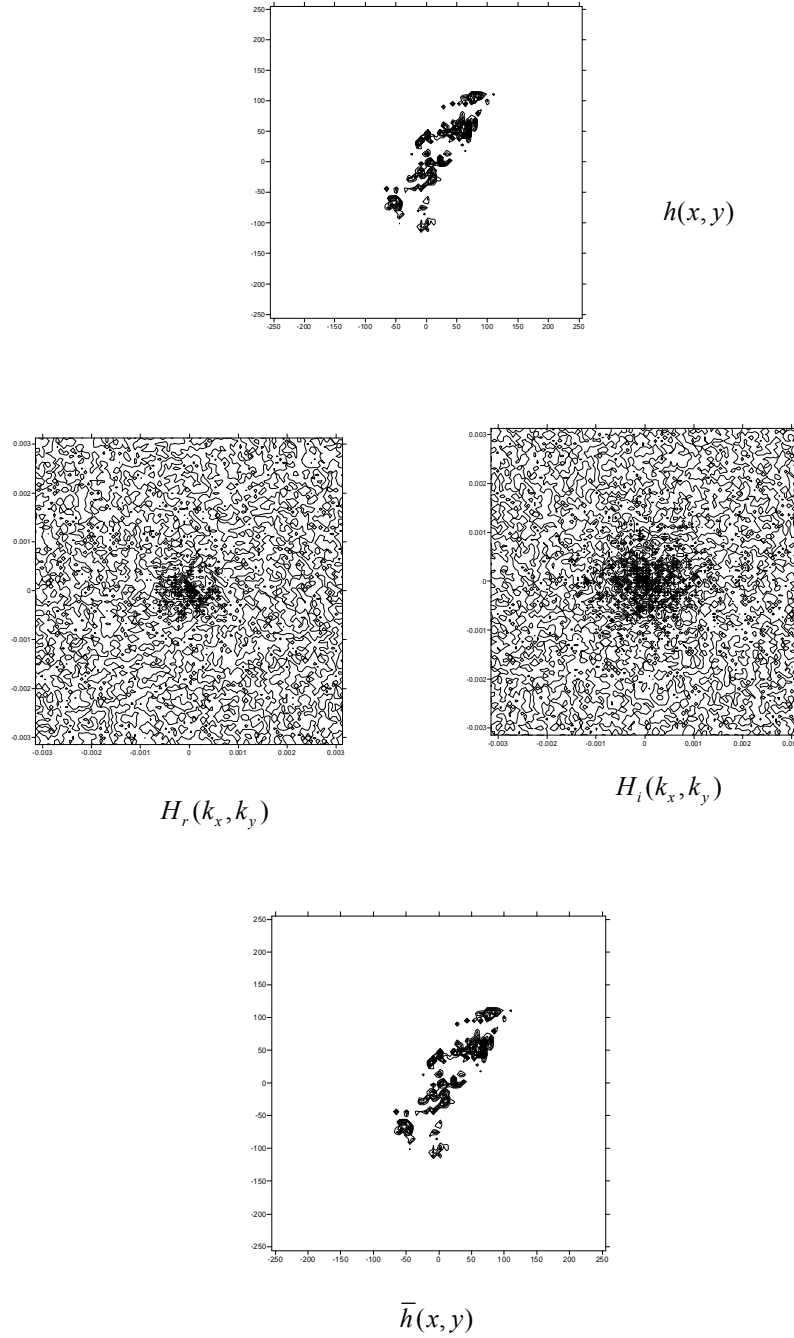
$h(x,y)$

$H_r(k_x, k_y)$

$H_i(k_x, k_y)$

$\bar{h}(x,y)$

Figure 1. The Fourier transform pair for terrain height in the real domain $h\left(x, y\right)$ and the complex terrain $H\left(k_x, k_y\right)$ of the wave number domain.

5.3 Examples of Smith Three-Layer Model Results using Theoretical and Real-World Terrain and Basic State

5.3.1 THEORETICAL RESULTS

To check the validity of the Smith Three Layer model implementation, four theoretical cases described in Smith's (2002) monograph were evaluated and compared with his published results. The calculations matched the published results and also serve to illustrate wave behavior for different combinations of stability, vertical shear, and terrain shape and terrain orientation. These four cases included (1) an axisymmetric hill with uniform wind velocity and stability, (2) a ridge line perpendicular to the mean flow direction with uniform wind velocity and stability, (3) an axisymmetric hill and ridge line with decreasing Scorer parameter (N/U) with height, and (4) the ridge line oriented 45° to the mean flow with decreasing Scorer parameter with height. The wind direction is constant with altitude for all cases. The inputs for the theoretical calculations are listed in Table 1.

For the hill shape, the equation representing the terrain height is

$$z(x, y) = h_{max} \exp\left[-(x/a)^2 - (y/b)^2\right] \quad \text{(m)}$$

where a and b are, respectively, the minor and major axes of the elliptical mountain shape. For the axisymmetric hill shape, $a = b$. In Figures 2 and 3, the planform analysis height is 5 km, while the planform analysis level is at 2 km in Figures 4 and 5. The vertical cross-section is valid for the red line positioned at y = 0. The results are displayed in terms of height deviation Δz from the mean or background height with h_{max} = 1000 meters.

Table 1.   Model Inputs for Theoretical Calculations Using Three Layer Model

	Terrain (a, b) hill/ridge	Stability N (s^{-1})	Wind Speed U (m/s)	Scorer Parameter N/U (m^{-1})	Absorption
Fig. 2	10 km	0.01	10	0.001	none
Fig. 3	10/50	0.01	10	0.001	none
Fig. 4a	2 km	0.012/0.008	10/22	0.0012/0.00036	$q = 0.93$
Fig. 4b	2/50	0.012/0.008	10/22	0.0012/0.00036	$q = 0.90$
Fig. 5a	2/50	0.012/0.008	8/22	0.0015/0.00036	$q = 0.93$
Fig. 5b	2/50/45°	0.012/0.008	10/22	0.0012/0.00036	$q = 0.90$

Figures 2 and 3 depict examples of terrain-induced waves in a hydrostatic environment since little energy will be put into wavelengths less than the hill radius. In Figure 2, the energy is confined to a downstream parabolic region while for the ridge case in Figure 3, the energy is found only in the vicinity of the ridge. In both cases, the wave phase tilts upstream into the wind. In Figure 4, the waves generated by the axisymmetric hill and ridge line are trapped by the change in wind speed and stability at 2 km, resulting in transverse wave modes (wave bands perpendicular to the shear vector) as well as a diverging parabolic wave for the axisymmetric hill. In Figure 5, the wind speed and

stability changes are introduced at a higher altitude associated with a deeper stable layer. This results in a short wavelength fundamental mode and a second, longer wavelength mode. In Figure 5b, the ridge is rotated clockwise 45° which results in two modes where the longer wavelength mode is rotated farther to the north than the shorter wavelength mode.
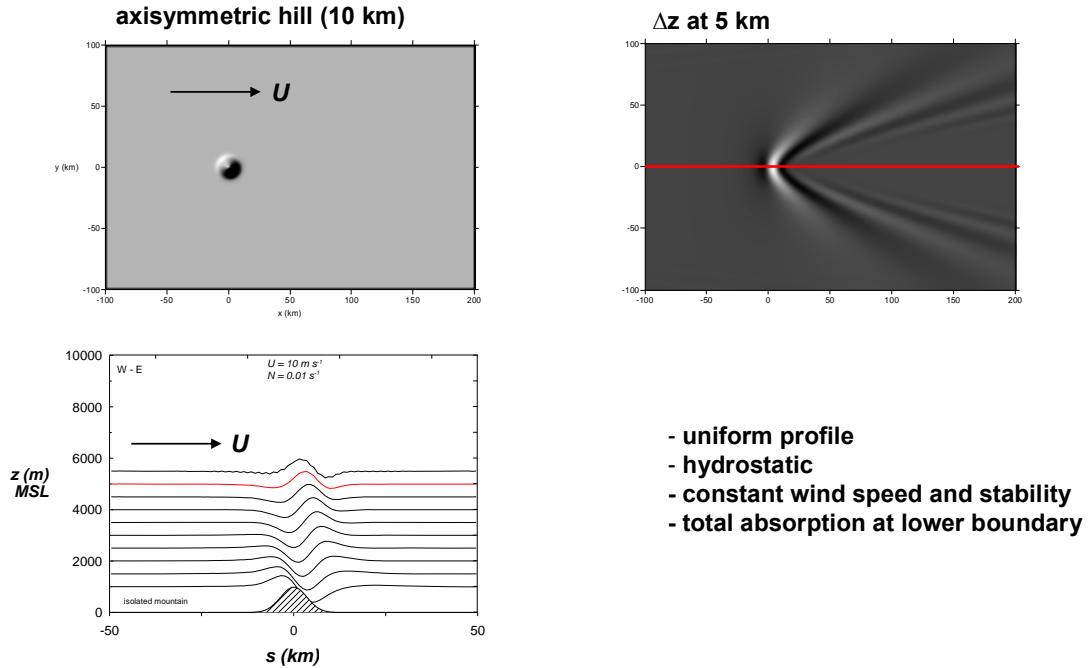

Figure 2. Gaussian hill profile (Witch-of-Agnesi) with constant wind speed and stability. Total absorption at lower boundary.
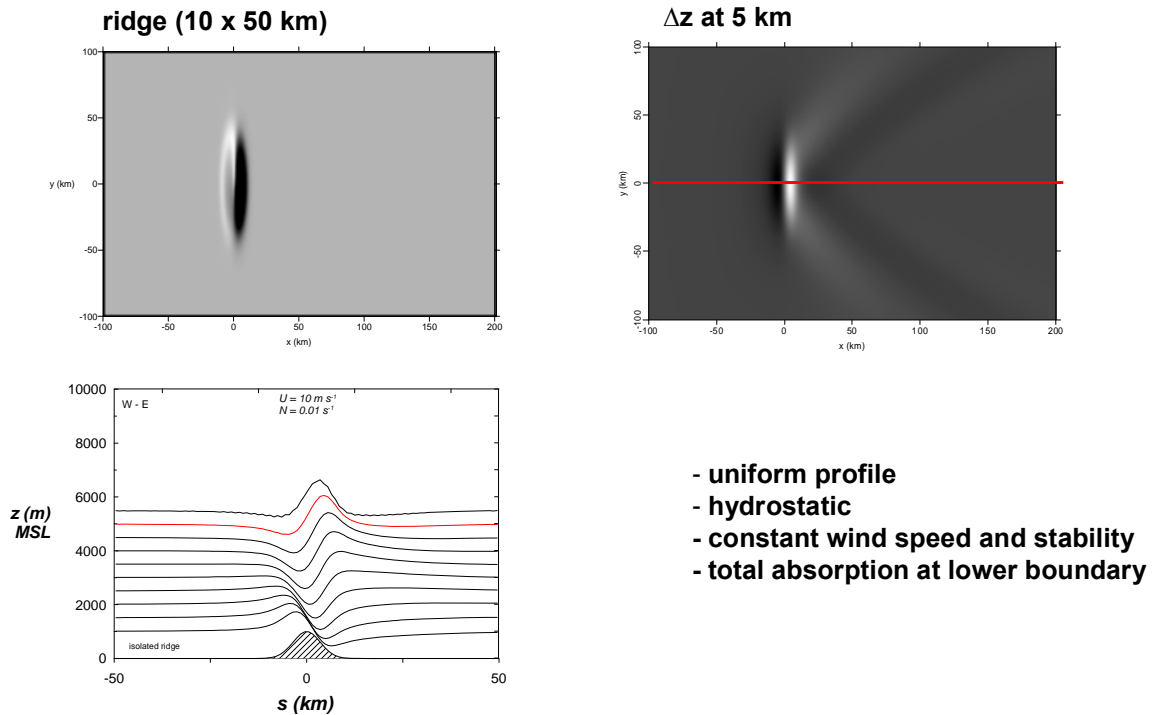

Figure 3. Ridge profile with constant wind speed and stability. Total absorption at lower boundary.

axisymmetric hill (2 km)

ridge (2 km x 50 km)

Δz at 2 km

$U_1 = 10 \ m \ s^{-1} \ U_2 = 22 \ m \ s^{-1}$
$N_1 = 0.012 \ N_2 = 0.08 \ s^{-1}$
$q = 0.9$

W - E

z (m)
MSL

long narrow ridge

s (km)

- **two-layer Scorer number (N/U) profile**
- **N/U decreasing with height (2.4 km)**
- **evanescent, trapped waves**

Figure 4. Two-layer wind speed and stability with reflection at lower boundary.
a. axisymmetric hill , q =0.93 (reflectivity factor) b. ridge (2 x 50 km), q=0.90

ridge (2 km x 50 km)

ridge (2 km x 50 km) rotated by 45˚

Δz at 2 km

y (km)

x (km)

$U_1 = 8 \ m \ s^{-1} \ U_2 = 22 \ m \ s^{-1}$
$N_1 = 0.012 \ N_2 = 0.08 \ s^{-1}$
$q = 0.93$

W - E

z (m)
MSL

long narrow ridge

s (km)

- **two-layer Scorer number profile**
- **lower layer depth increased to 4 km**
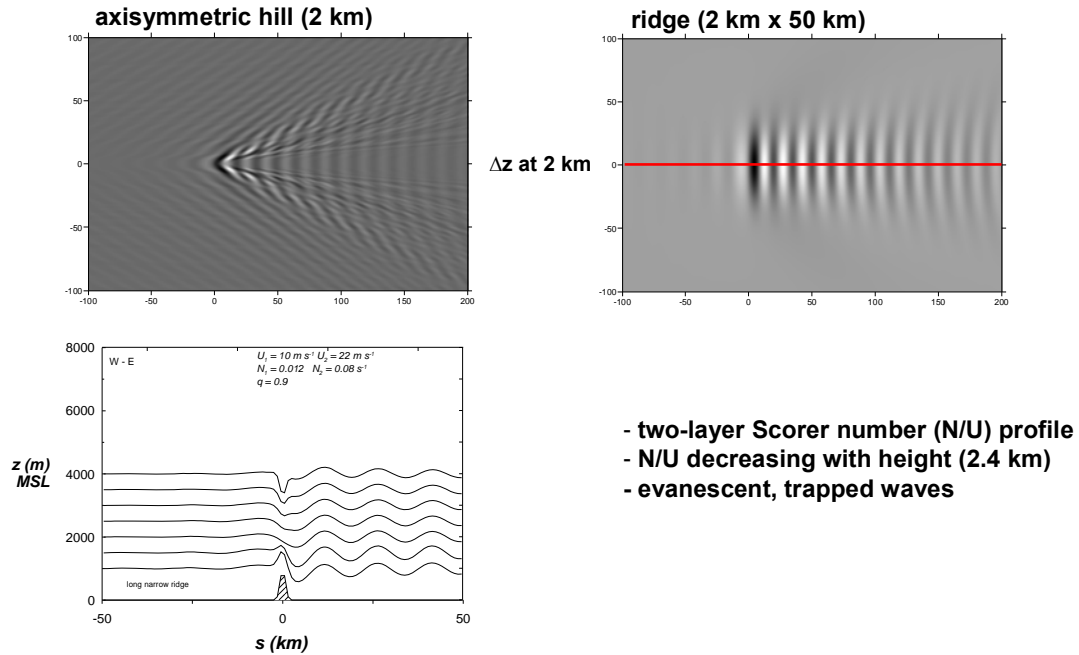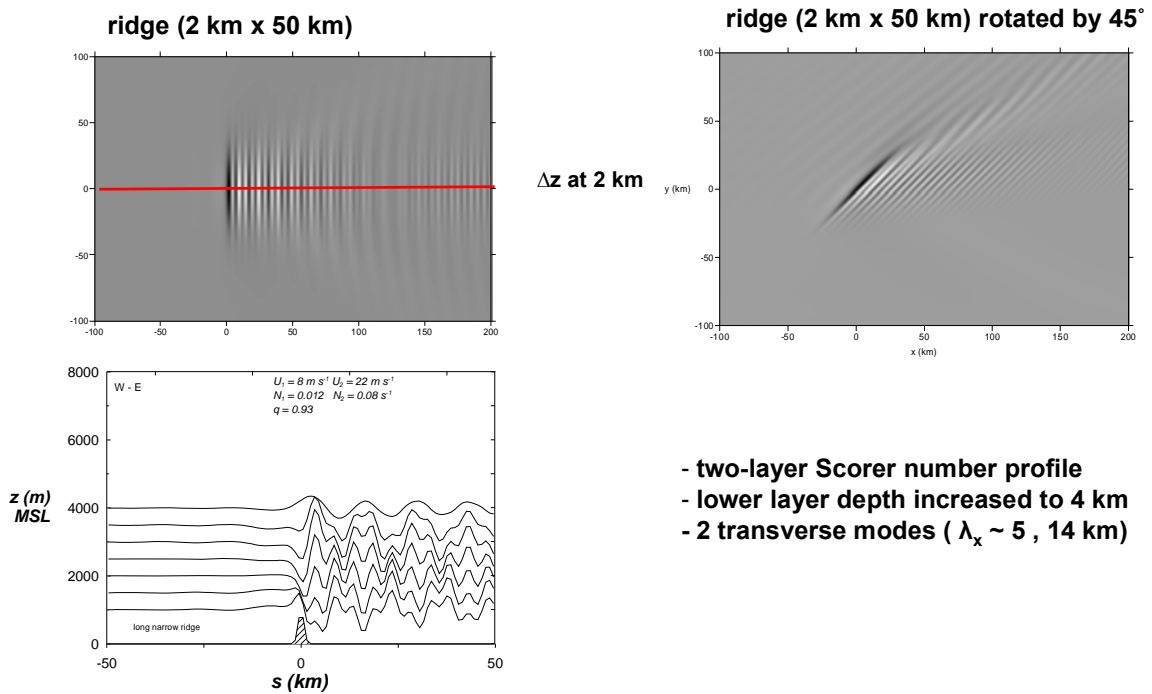- **2 transverse modes ($\lambda_x \sim 5$, 14 km)**

Figure 5. Two-layer wind speed and stability with reflection at lower boundary.
a. ridge (2 x 50 km) , q =0.93 (reflectivity factor) b. ridge (2 x 50 km) rotated by 45˚, q=0.90

5.3.2 REAL-WORLD TERRAIN AND BASIC STATE

Calculations using the Smith Mountain Three Layer Wave Model are illustrated using real-world terrain over the French Alps for a case study described by Smith et al (2002) during the 1999 Mesoscale Alpine Programme (MAP) campaign. This is the same terrain field depicted in the terrain padding example described earlier. The terrain field is centered near latitude 46° N, longitude 7° E. A three layer model profile of wind velocity and static stability is used which is based on rawinsonde and dropsonde measurements taken at 1200 UTC on 2 November 1999.   Given a stagnant layer top of 2.5 km above mean sea level (MSL) and a reflectivity factor $q = 0.90$, Table 2 lists the layers and their mean static stability and mean wind velocity characteristics used for the model input.

Table 2. Three-Layer Model Input for 2 November 1999, French Alps

	base (km)	N (s^{-1})	ddd/ff (° /, m/s)
Layer 1	2.5	0.012	220/15
Layer 2	7.0	0.009	220/21
Layer 3	12.0	0.020	220/31

Note that the wind direction is constant with height while the speed varies between layers.

Figure 6 depicts the model height perturbation solution $\eta(x,y)$ in meters at $z = 7.5$ km MSL in the horizontal plan view (top) and $\eta(x,y,z)$ along a SW – to – NE cross-section (bottom). The cross-section horizontal position is depicted by the blue dashed line on the plan view. The axis of the bow wave pattern resulting from the terrain height distribution lies parallel to the mean wind flow and a variety of transverse wave patterns are also evident in the flow. The vertical cross-section in the lower half of the figure indicates the amplitude of the height perturbations at each level and the tendency for these perturbations to tilt upstream (to the left in the bottom figure).

5.3.3 COMPARISON WITH BALLOON MEASUREMENTS

To gain further appreciation into the validity of the Fourier calculations, a comparison of model vertical velocity w with balloon-derived air vertical velocity was accomplished. Basic states for the Fourier calculations were constructed using Global Forecast Spectral Model archives for two different times and locations where high resolution (~ /1.5 second sample rate) balloon-borne rawinsonde measurements were made in the vicinity of mountains. The locations and times for the balloon launches were (1) the island of Hawaii with balloon launch from Bradshaw Army Airfield (19° 47' N, 155° 33′ W) on 12 December 2002 near 06 UTC and (2) the Provence Region of France in the southern Alps with balloon launch from the OHP Observatory (44° N, 5° 42′ E) on 24 November 2004 around 00 UTC.

km (north)

Δz at 7.5 km MSL

cross-section of z + Δz

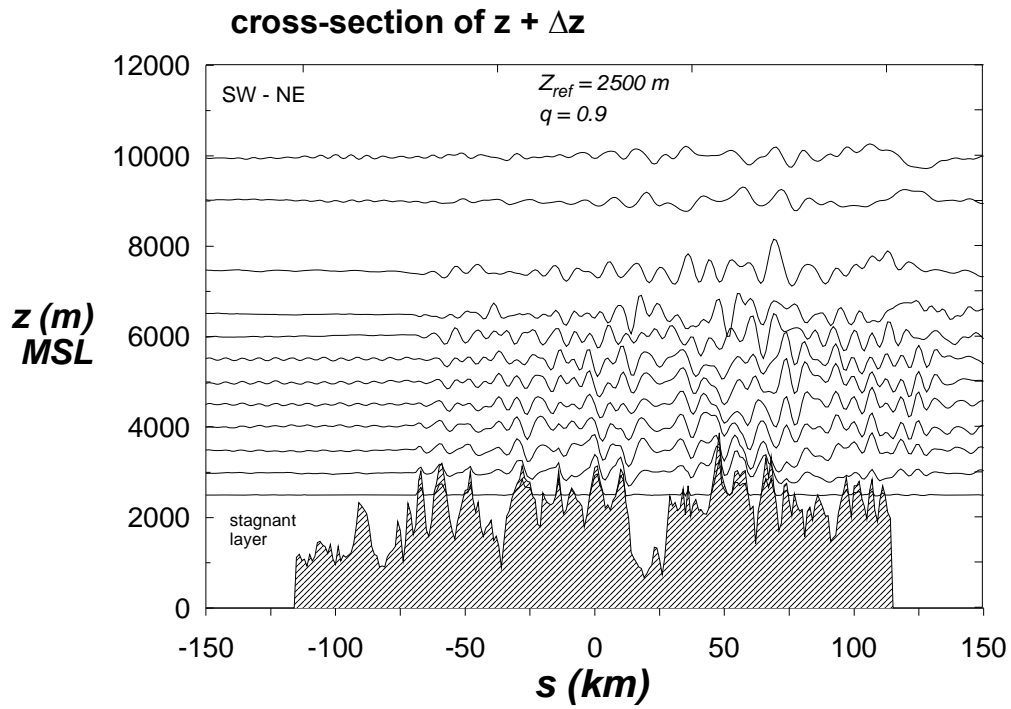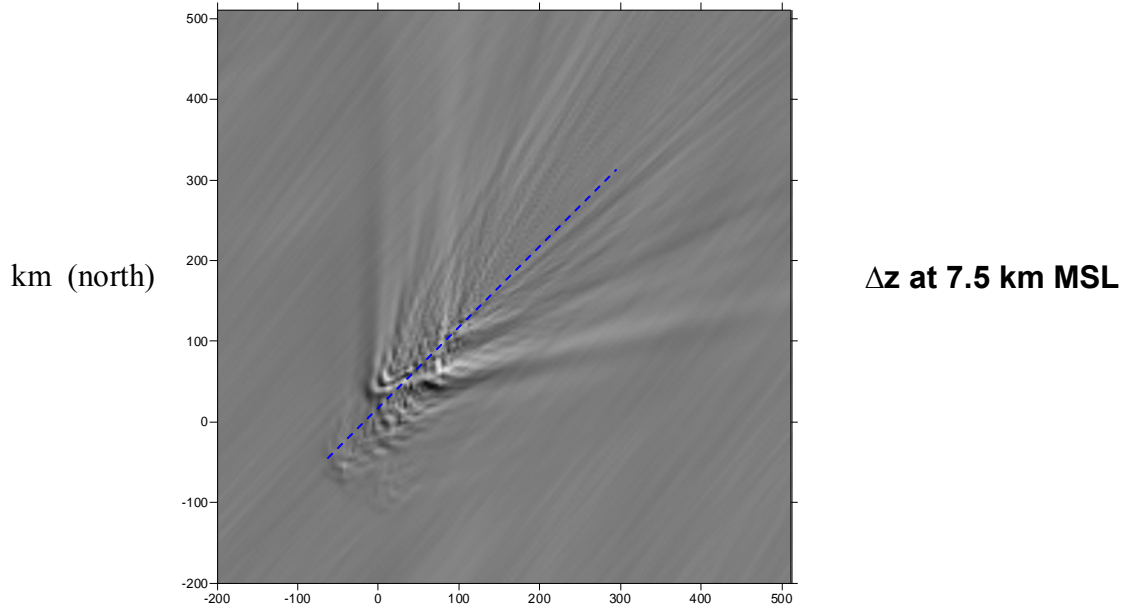$Z_{ref} = 2500 \ m$
$q = 0.9$

SW - NE

z (m) MSL

stagnant layer

s (km)

Figure 6. Height perturbations $\eta(x, y)$ displayed for French Alps MAP case with basic state as described in Table 1 for z = 7.5 km MSL (top) and for SW- NE vertical cross-section at bottom. The cross section is along the line denoted by the dashed blue line on the plan view.

The basic state atmosphere over Hawaii was characterized by weak northeast trade flow at low altitudes backing toward stronger northwest flow above 10 km. A trade inversion existed with the inversion base near 1.5 km MSL. For the Provence atmospheric background, steady northerly flow prevailed at all levels with some weak backing of the wind with height. The basic states for the two locations are listed in Tables 3 and 4 where $\bar{U}$ represents the west-to-east wind speed component and $\bar{V}$ represents the south-to-north wind speed basic state component.

Table 3. Three-Layer Model Specifications for Hawaii
12 December 2002   06 UTC

site elevation: 1887 m
$q = 0.90$ (boundary reflectivity) ; stable layer : 0 – 1 km MSL

	base (km)	$N\,(s^{-1})$	U (m/s)	V (m/s)
Layer 1	1.0	0.010	- 10.0	- 5.0
Layer 2	9.0	0.008	+20.0	-10.0
Layer 3	16.0	0.020	+ 2.0	- 2.0

Table 4. Three-Layer Model Specifications for Provence
24 November 2004 00 UTC

site elevation: 650 m
q = 0.90 (boundary reflectivity) ; stable layer : 0 – 0.6 km MSL

	base (km)	$N\,(s^{-1})$	U (m/s)	V (m/s)
Layer 1	0.6	0.016	- 0.7	- 3.9
Layer 2	3.1	0.008	+ 1.4	-7.8
Layer 3	10.5	0.020	+ 1.6	- 9.1

A high-pass filter technique was used to calculate the observed vertical velocity perturbations about the mean balloon rise rate (Murphy, 2006) using standard digital processing techniques. The Nyquist frequency of the balloon sampling rate is much higher than the spatial frequencies associated with the mountain waves. The mean balloon rise rate is determined, using the hydrostatic assumption, from the sonde pressure time tendency $\Delta p/\Delta t$. Air pressure and temperature are sampled at 1- to 2-second intervals during balloon ascent. Horizontal wind velocities, reported at a comparable sampling interval by the rawinsonde using GPS-derived Doppler shift and smoothed using a Gaussian window filter, are also used to determine the three-dimensional balloon trajectories. The comparison between balloon and model vertical velocities was performed from the surface to 15 km above sea level (MSL). For these cases, the horizontal balloon drift during the ascent to 15 km was on the order of 20 to 40 km.

The model vertical velocity w along the balloon trajectory $s(x, y, z)$ used in the comparison is interpolated from the three-dimensional Fourier model output grid using a vertical grid spacing $\Delta z = 50$ m and horizontal grid spacing $\Delta x = \Delta y = 1$ km. 15 km MSL
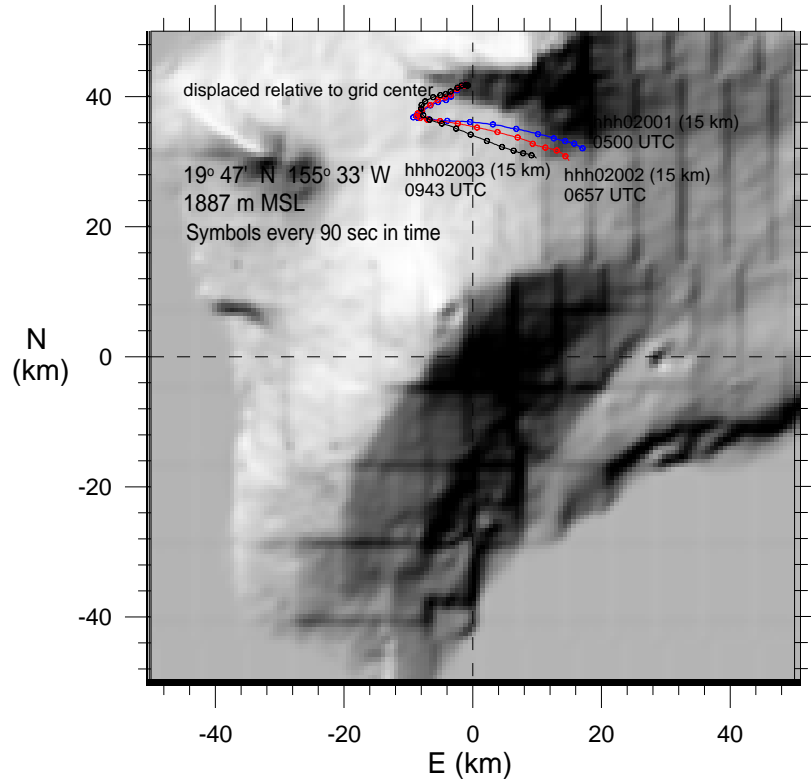
Figure 7a. Terrain relief overlain with balloon trajectories tracked to 15 km for Hawaii, 12 December 2002.
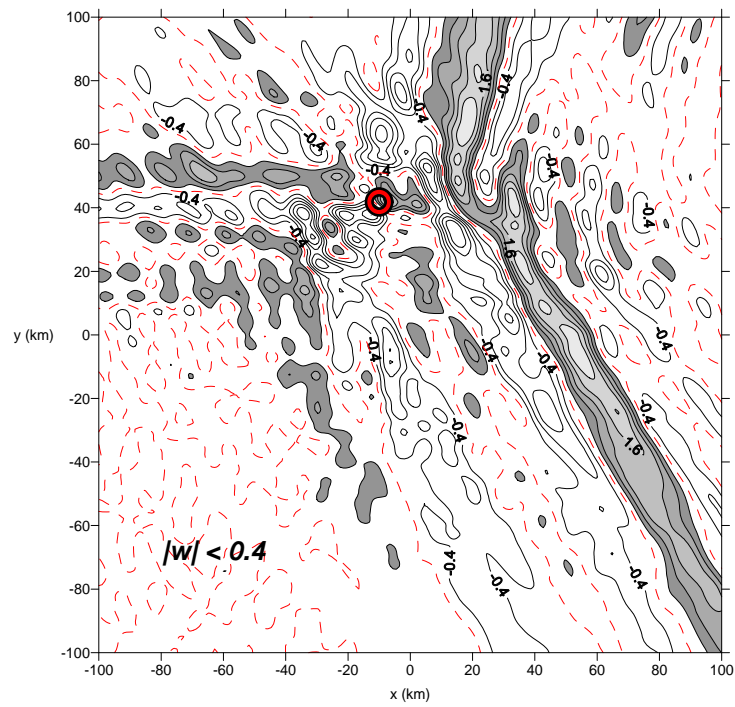

Figure 7b. 3 Layer Model vertical velocity contours over Hawaii at 12 km MSL. The contour interval is 0.4 m/s. The red ring marks the balloon launch location.
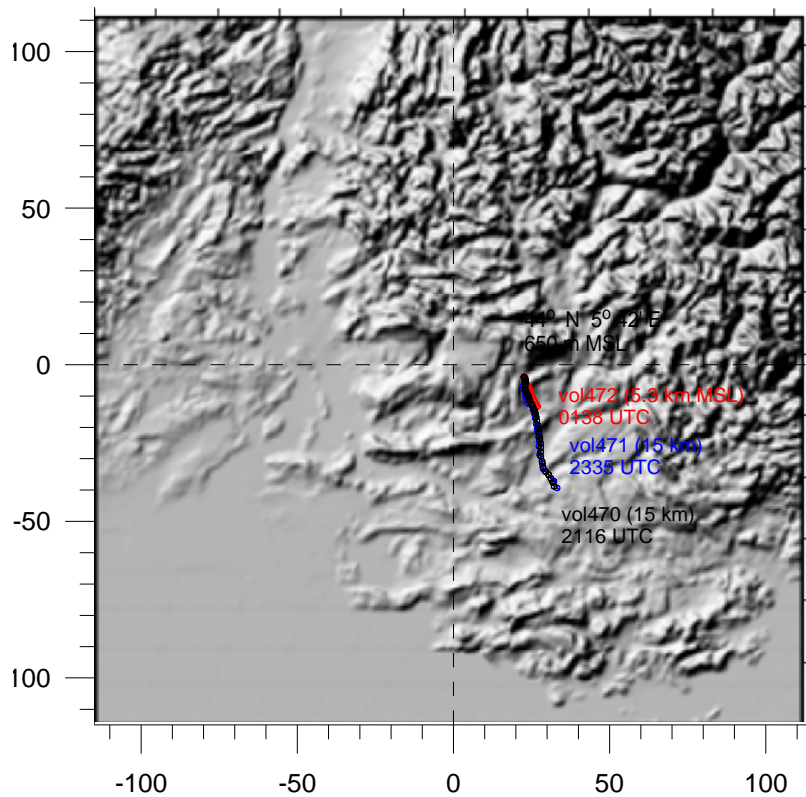
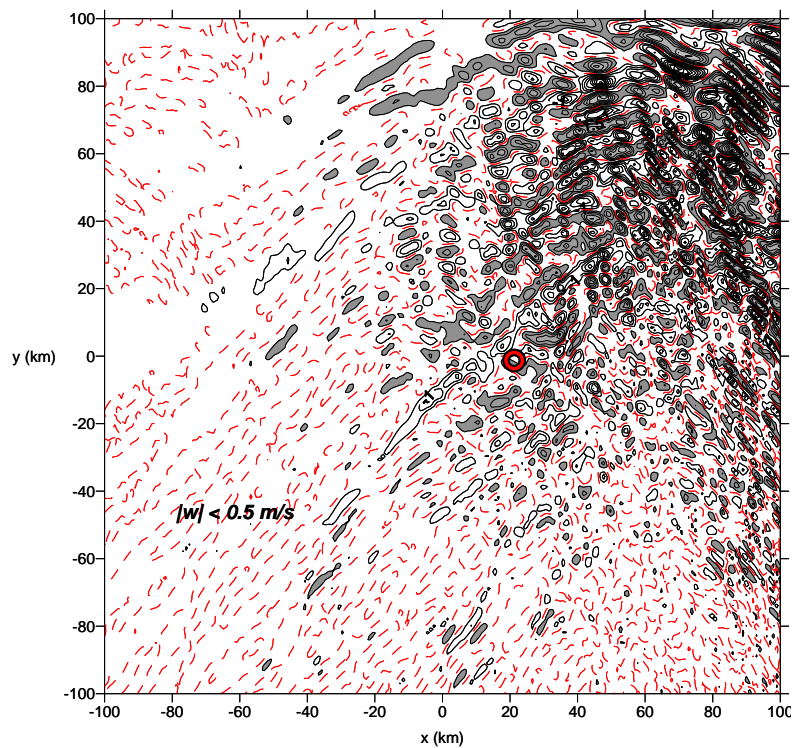Figure 8a. Terrain relief overlain with balloon trajectories tracked to 15 km in France, 24 November 2004.

Figure 8b. 3 Layer Model vertical velocity contours over Provence at 12 km MSL. The contour interval is 0.5 m/s. The red ring marks the balloon launch location.
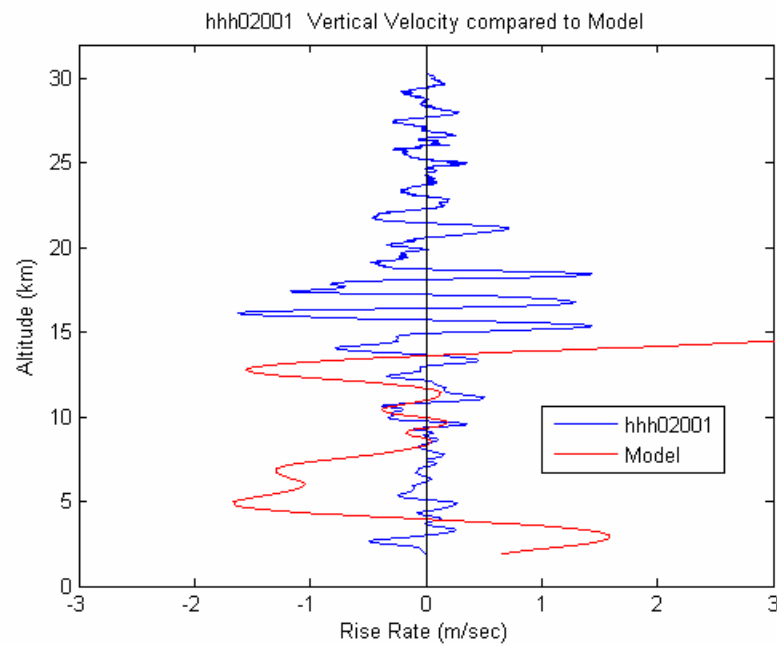
Figure 9a. Balloon-derived vertical velocity (blue) compared with 3 Layer model output (red) for sonde launch at 12 December 2002 0500 UTC from Bradshaw AAF, HI
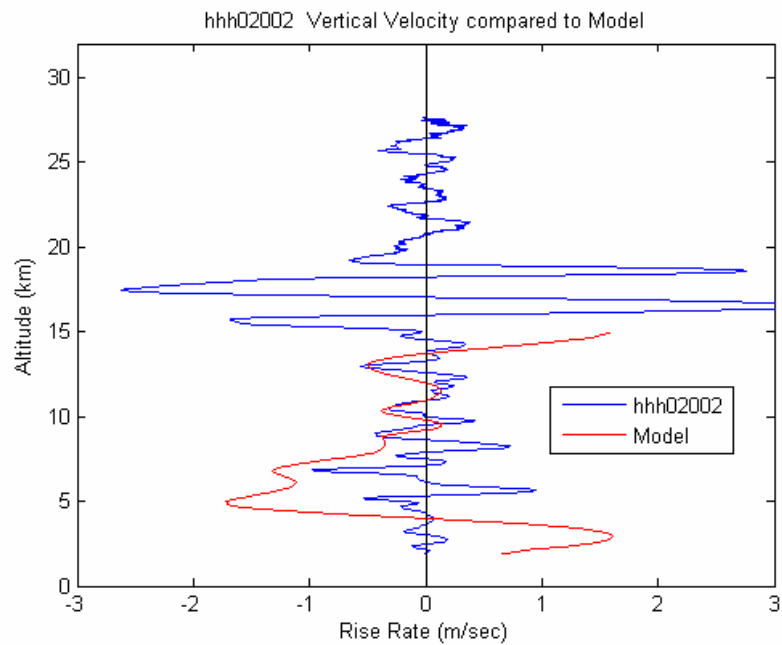

Figure 9b. Balloon-derived vertical velocity (blue) compared with 3 Layer model output (red) for sonde launch at 12 December 2002 0657 UTC from Bradshaw AAF, HI

Figure 10a. Balloon-derived vertical velocity (blue) compared with 3 Layer model output (red) for sonde launch at 23 November 2004 2335 UTC from OHP Observatory, France
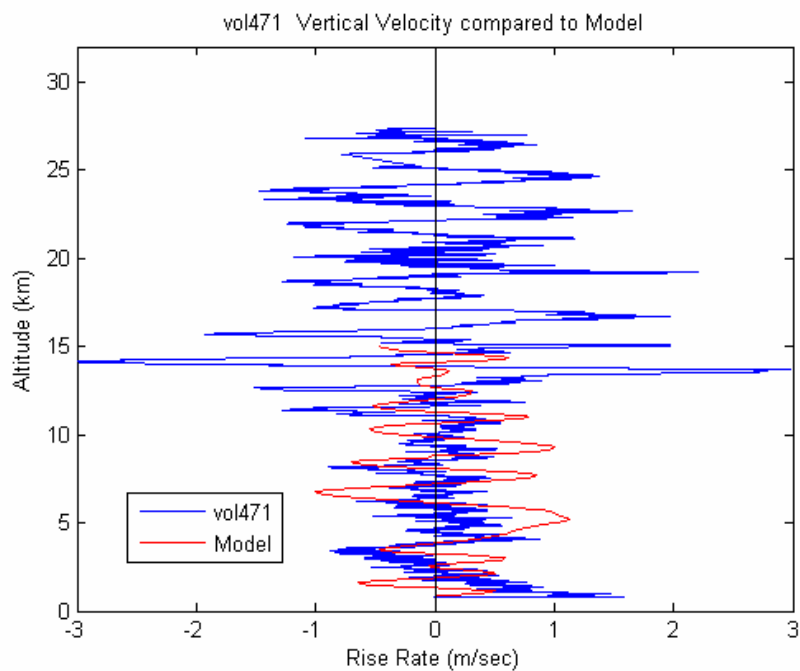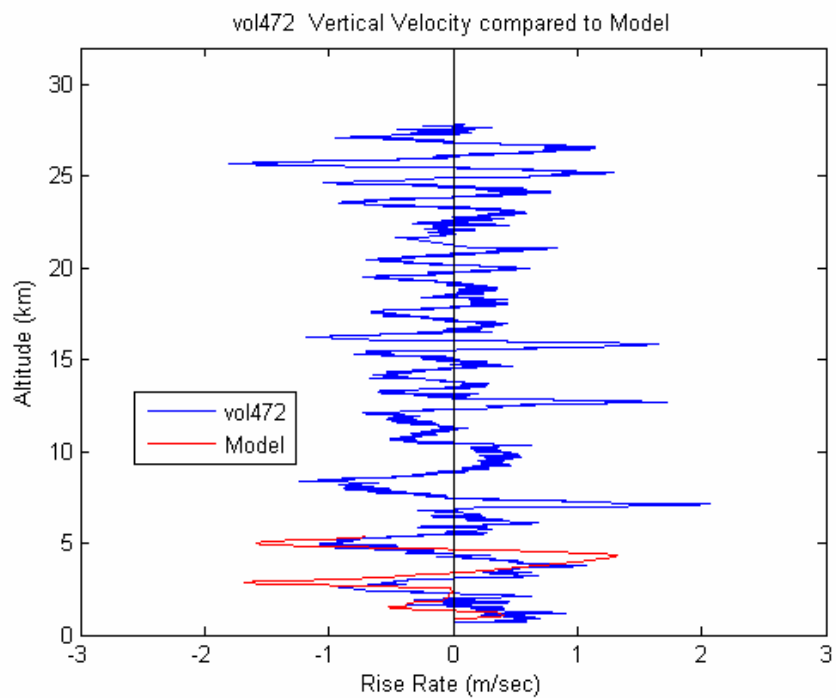

Figure 10b. Balloon-derived vertical velocity (blue) compared with 3 Layer model output (red) for sonde launch at 24 November 2004 0406 UTC from OHP Observatory, France

is set as the top level of model calculation for these comparisons, which equates to a less than 50 minute period using a mean balloon ascent rate of 5 m/s.

Figures 7 and 8 depict the terrain relief, horizontal balloon trajectories, and model vertical velocity output at 12 km MSL for Hawaii and Provence, respectively. The same axis scale reference is used for the terrain and vertical velocity plots in each figure. These figures illustrate the complexity of both the underlying terrain and the associated model vertical velocity fields generated using the terrain and atmospheric background.

Figures 9 and 10 show the comparison of the model and balloon-derived vertical velocities for the Hawaii and Provence launches, respectively. For the Hawaii case (Figure 9), the model magnitudes were much larger than the balloon-derived values below 8 km but showed better agreement in sign and magnitude between 9 and 15 km MSL. Below 15 km, the maximum measured vertical velocities are on the order of +/- 1 m/s while the model predicted velocity magnitudes are on the order of +/- 2 m/s. There was also better agreement in the sign of the vertical velocity above 8 km compared to lower altitudes.

For the Provence case study, reasonable agreement in magnitude and sign were found between the observed and model vertical velocities (Figure 10) although the model was somewhat out-of-phase with the observed during the first launch (2335 UTC). For the two launches, the magnitude of the observed and model vertical velocities varied between approximately +/- 1 m/s. Due to poor wind data acquisition during the second launch (0406 UTC), the balloon trajectory, and thus, the model comparison, ends just above 5.4 km MSL.

6. BROUTMAN CONTINUOUS MOUNTAIN WAVE FORECAST MODEL 3 (MWFM-3)

Three principal journal articles describe MWFM-3, the intended successor to MWFM-2 (Marks and Eckermann, 1995). They are Broutman et al, 2002 ; Broutman et al, 2003 ; and Broutman et al, 2006. The first article (2002) deals with stationary, hydrostatic, vertically-propagating wave modes while the second article (2003) deals primarily with trapped non-hydrostatic modes involving steady-state solutions. The most recent article (2006) describes transient or time-dependent solutions. These solutions are all demonstrated using a shallow quasi-Gaussian shaped-hill with a height of 100 m for the lower boundary. This shape, sometimes referred to as the "Witch-of-Agnesi" and easily represented in the wave number domain by an algebraic expression, is used to induce small magnitude stationary perturbations in the height field. From these height perturbations, vertical and horizontal velocities are also diagnosed using analytical expressions.

6.1 Governing Equations for MWFM-3   (after Broutman et al, 2003):

The intrinsic frequency σ and dispersion relation for the vertical wave number m, respectively, are:

$$\sigma\left(k_x, k_y, z\right) = -k_x \bar{U}(z) - k_y \bar{V}(z) = \frac{(k_x^2 + k_y^2)^{\frac{1}{2}} N(z)}{\left(k_x^2 + k_y^2 + m\left(k_x, k_y, z\right)^2\right)^{\frac{1}{2}}} \quad \text{(rad/s)} \tag{13}$$

For non-hydrostatic wave modes:

$$m\left(k_x, k_y, z\right) = \left[\left(k_x^2 + k_y^2\right)\frac{N^2 - \sigma^2}{\sigma^2}\right]^{\frac{1}{2}} \quad \text{(rad/m)} \tag{14}$$

For hydrostatic wave modes:

$$m\left(k_x, k_y, z\right) = \left[\left(k_x^2 + k_y^2\right)\frac{N^2}{\sigma^2}\right]^{\frac{1}{2}} \quad \text{(rad/m)} \tag{15}$$

The height perturbation $\hat{\eta}$ is composed of the sum of vertically propagating $\hat{\eta}_{pr}$ and trapped wave $\hat{\eta}_{tr}$ components over all wave numbers:

$$\hat{\eta}\left(k_x, k_y, z\right) = \hat{\eta}_{pr}\left(k_x, k_y, z\right) + \hat{\eta}_{tr}\left(k_x, k_y, z\right) \quad \text{(m}^3\text{/rad)}$$

From this, the vertical and horizontal velocity in the transform domain can then be determined

$$\hat{w}\left(k_x, k_y, z\right) = -i\sigma\hat{\eta}\left(k_x, k_y, z\right) \quad \text{(m}^3\text{ s}^{-1}\text{)}$$

$$\hat{u}\left(k_x, k_y, z\right) = \frac{-ik_x m\hat{w}}{\left(k_x^2 + k_y^2\right)}$$

The buoyancy frequency turning point height $z_t = f(k, N, \bar{U})$ is a function of horizontal wave number or mode, static stability, and horizontal wind velocity and is defined locally to be where intrinsic frequency is equivalent to the static stability or $\sigma = N$. This also serves as a caustic point (Lighthill, 1978) since the turning point acts as the boundary for a trapped-wave region.

According to Lighthill (1978), a caustic is a boundary between a region with a complicated wave pattern due to interference between two groups of groups of waves, and a neighboring region including no waves. Both critical layers and turning points act as caustics, although turning points only occur with non-hydrostatic modes. The MWFM-3 model described here can only handle the cases of zero or one turning point in the vertical for each wave number mode.

6.2 Vertically propagating wave mode: $\tilde{\eta}_{pr}$

The vertically-propagating wave mode is defined as the contribution to the upward propagating wave field for each mode at or below a turning point height z_t. (z_t does not necessarily exist for each mode, e.g. for hydrostatic modes.) The phase angle for vertically propagating waves is

$$\phi_p\left(k_x,k_y\right)=-\int_0^z m\left(k_x,k_y,z\right)dz \quad \text{(radians)} \tag{16}$$

where the integral's sign is assigned the following meanings:

(-) sign for m indicates upward group velocity and downward phase velocity
(+) sign for m indicates downward group velocity and upward phase velocity

Differentiating Eq. (13) with respect to m, the vertical wave group velocity c_g is written as:

$$c_g\left(k_x,k_y,z\right)=\frac{\partial \sigma}{\partial m}=\frac{-\left(k_x^2+k_y^2\right)^{\frac{1}{2}}\cdot N(z)\cdot m}{\left(k_x^2+k_y^2+m^2\right)^{\frac{3}{2}}} \quad \text{(m s}^{-1}) \tag{17}$$

The vertical flux of wave action $G\left(k_x,k_y,z\right)$ is expressed in terms of static stability (the square of the Brunt-Vaisala frequency, N^2), vertical group velocity, and intrinsic frequency:

$$G\left(k_x,k_y,z\right)=N^2\left(z\right)c_{g3}\big/\sigma\left(k_x,k_y\right) \quad \text{(kg m}^{-2}\text{ s}^{-2}) \tag{18}$$

The expression for height perturbation for vertically propagating modes, using the general form of Eq. (1), then becomes

$$\hat{\eta}_{pr}\left(k_x,k_y,z\right)=\hat{h}\left(k_x,k_y\right)\left[G_0/G\right]^{\frac{1}{2}}e^{i\phi_p} \quad \text{(m}^3\text{ rad}^{-1}) \tag{19}$$

where $\quad \hat{h}\left(k_x,k_y\right)=\dfrac{1}{2\pi}\int_{-\infty}^{\infty}\int_{-\infty}^{\infty}h\left(x,y\right)e^{ik_xx}e^{ik_yy}dx\,dy$ (m^3 rad^{-1}) and the "0" subscript denotes the expression for a variable that is valid at $z=0$.

For vertically-propagating wave modes, solution methods are straightforward and involve simply the vertical integration of the dispersion relation m from the surface to the desired altitude z . Examples of these solutions are displayed in Figure 11. A 20 km radius hill, centered at the origin with a height of 100 m, is used for the lower boundary. Contour plots are produced for the two-dimensional distribution of vertical and horizontal velocity at altitudes equal to 2.1 km and 6.3 km, and compared with published results from Broutman et al (2002). The blue values in parentheses represent the published maxima and minima while the black values represent the AFRL model calculation results. The phase functions used in these examples are evaluated analytically. Close agreement between published and calculated magnitudes show the similarity in application of Fourier methods even though the grid dimensions differed significantly -- 2^8 for Broutman et al (2002) vs. 2^{10} for the results displayed in Figure 11.

(a)

u' (m/s)
z = 2.1 km

-0.43, +0.30
(-0.38, +0.35)

(b)

w' (m/s)
z = 2.1 km

-0.036, +0.034
(-0.035, +0.030)

(c)

u' (m/s)
z = 6.3 km

-0.25, +0.26
(-0.25, +0.26)

(d)

w' (m/s)
z = 6.3 km
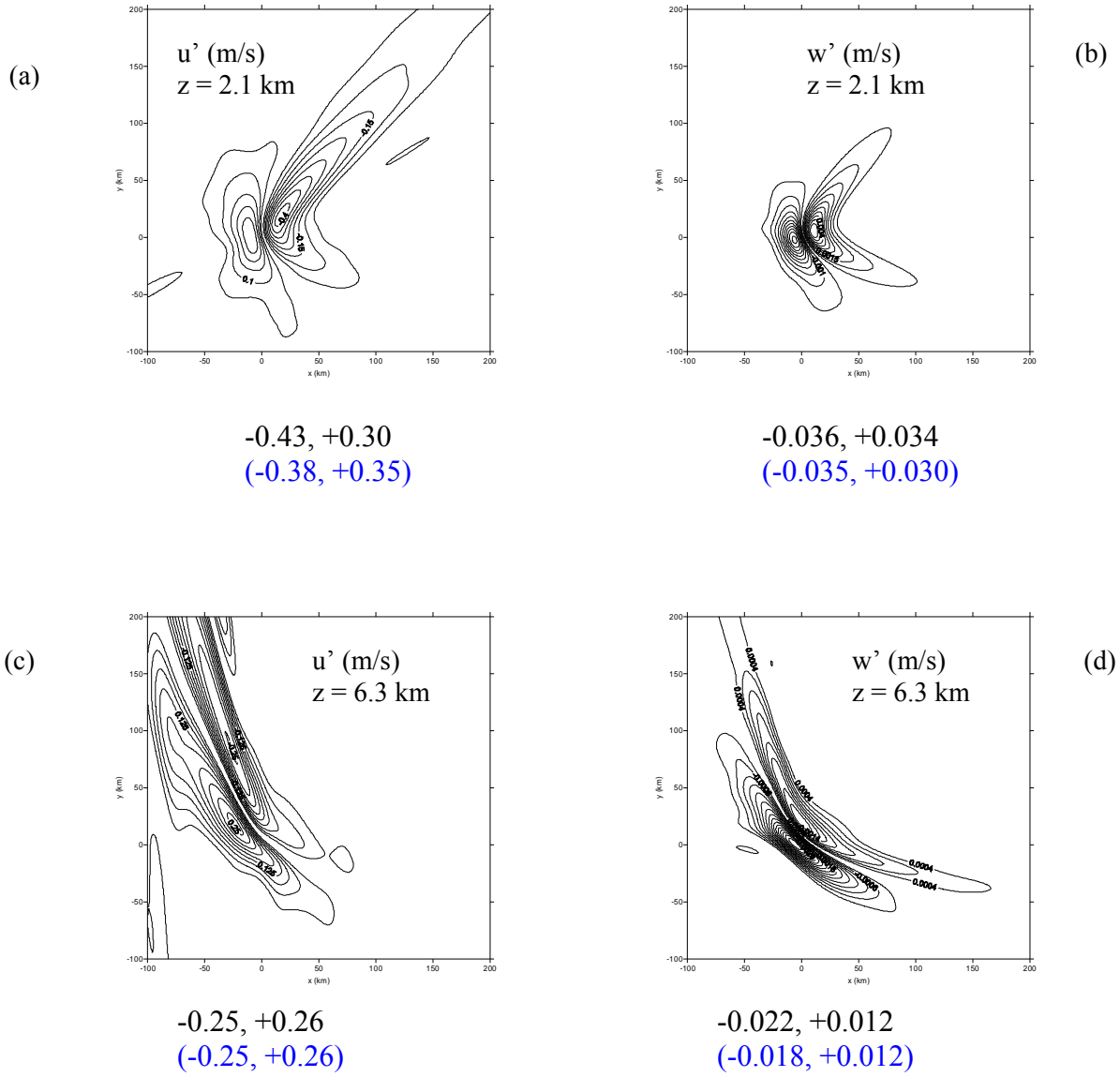
-0.022, +0.012
(-0.018, +0.012)

Figure 11. Calculations of hydrostatic vertically-propagating modes using MWFM-3
            Values in parentheses are published results (Broutman et al, 2002)

numerical specifications:
$\Delta x = \Delta y = 1000$ m
bandwidth: 6.28×10^{-3} rad/m
wave number grid: 1024 x 1024

atmospheric specification:
$u(z) = U_0 \cos(\pi z/H)$; $v(z) = U_0 \sin(\pi z/H)$; $H = 12$ km ; $U_0 = 10$ m/s
$N = 0.0113$ s^{-1} ; Richardson number ~ 19 ; hill radius = 20 km, height = 100 m

6.3 Vertically-trapped waves: $\tilde{\eta}_{tr}$

For vertically-trapped waves, the "long-time" steady-state solution requires invocation of the Airy function $Ai(\rho)$ where the phase functions form its argument, ρ, and which may be complex. The Airy function and its determination are described in Section 6.4 and in Appendix B. Solutions which correct for the trapped waves or caustics are referred to as "uniform" solutions (Broutman and Rottman, 2004) due to their uniformly valid behavior in the vicinity of singularities.

In a general form, the trapped wave solution is:

$$\hat{\eta}_{tr}\left(k_x,k_y,z\right)=\hat{h}\left(k_x,k_y,z\right)\left[G_0/G\right]^{\frac{1}{2}}\left[\rho/\rho_0\right]^{\frac{1}{4}}\times\frac{Ai(\rho)}{Ai(\rho_0)} \tag{20}$$

The phase functions ϕ are expressed as

$\phi_1=-\int_0^{z_t}m\,dz$ for a ray incident upon the caustic level z_t

$\phi_2=\pm\int_{z_t}^{z}m\,dz$ for a ray reflected from the caustic level z_t

where

$\rho=\pm\left[\frac{3}{4}\left(\phi_1-\phi_2\right)\right]^{\frac{2}{3}}$, $Ai(\rho)$ is the Airy function, and ρ can be real or complex

and $\rho = 0$ if $z = z_t$

         $\rho < 0$ if $z < z_t$

         $\rho > 0$ if $z > z_t$

         $\rho = \rho_0$ for $z = 0$, $\rho_0 = -\left[\frac{3}{2}\phi_1\right]^{\frac{2}{3}}$

For the solutions described below, ρ is treated as a real function and ρ_0 is complex.

The phase integral sign convention follows the same relation as was used for vertically-propagating modes:

+ upward phase velocity
   downward group velocity

- downward phase velocity
   upward group velocity

The relevant features of Broutman et al (2003) for stationary trapped wave modes were replicated to gain understanding into the trapped wave mode behavior. The calculations use the "Case II" specification of Wurtele et al (1987). This case uses a linear increase of zonal wind speed with height and a fixed value for static stability ($N = 0.01$ s^{-1}). A 2.5 km-radius hill centered at the origin with height of 100 m is used for the lower boundary. All calculations are for trapped wave modes and use complex functions except where indicated. The essential results are presented in Figures 12 through 16.

Figure 12 shows that calculations of turning point height z_t as a function of horizontal wavelength compare well with the published results. For calculations at all wavelengths, if $z_t = 0$, then the eigenfunction η_{tr} is treated as zero at that wavenumber. The turning point height is also treated as zero in MWFM-3 once it becomes less than zero. The turning point height will eventually become zero or negative when the spatial wave number exceeds a certain value, as shown in Figure 12. For the MWFM-3 model calculations, these zero or negative turning point height wavenumber values are skipped.

The normalized vertical eigenfunction calculations for trapped wave modes using MWFM-3 plotted in Figures 13a and 13c agree reasonably well with those published. However, there is a sign reversal in Figure 13b which was not replicated and which may contribute to some of the differences seen in Figure 14. The eigenfunctions' appearance also became slightly smoother with altitude when the phase function integrals were evaluated analytically rather than numerically.

In Figure 14, the eigenfunction modulus contour patterns, as a function of spatial wavenumber, match but there is slightly more damping of the peaks in the calculations for the uniform solution compared to published values. Here, the 15 km mode magnitude dominates the 33 km mode. The uniform solution damping with height is due to the addition of a small imaginary wavenumber component, $k_i = 5 \times 10^{-6}$ rad/m. Additional experiments (not shown) indicate the eigenfunction magnitude and wavenumber positions are somewhat sensitive to the size of the imaginary wavenumber component.

Figure 15 shows that the vertical velocity cross-sections for the 1-D Fourier transform solution match well the published values. The maximum published values are shown parenthetically. The vertical velocity is calculated at 1 km vertical increments. The calculated vertical cross-section using the 1-D Fourier transform and the 2-D inverse Fourier transform displayed in plan form (Figure 16 a) matches the dominant ~ 15 km mode shown in Figure 14 and Wurtele et al's linear analysis for case II. Evidence of a 30 – 35 km mode is seen near an altitude of 15 km in Figure 15.

Figure 16 shows a comparison of the MWFM-3 trapped wave vertical velocity pattern for the 2-D plan view. Broutman et al (2003) attribute the ship bow behavior and modulus diminishment with distance downstream of the hill to the imaginary wave number component. Both calculations show excellent agreement in amplitude and phase. The published maximum and minimum values are shown in parentheses.

Two modifications were required beyond what is cited in the Broutman et al (2003) article to produce the trapped wave modes that dissipate downstream with distance. These were determined from correspondence with Dr. Broutman:

The primary modification was that the phase function ρ_0 should be maintained as a complex argument of the complex Airy function $Ai(\rho_0)$ in Eq. (20). To avoid singularities associated with the resonant modes or zeroes of the Airy function, a small imaginary component $0.01i$ is added to ρ_0. However, ρ is maintained as the real
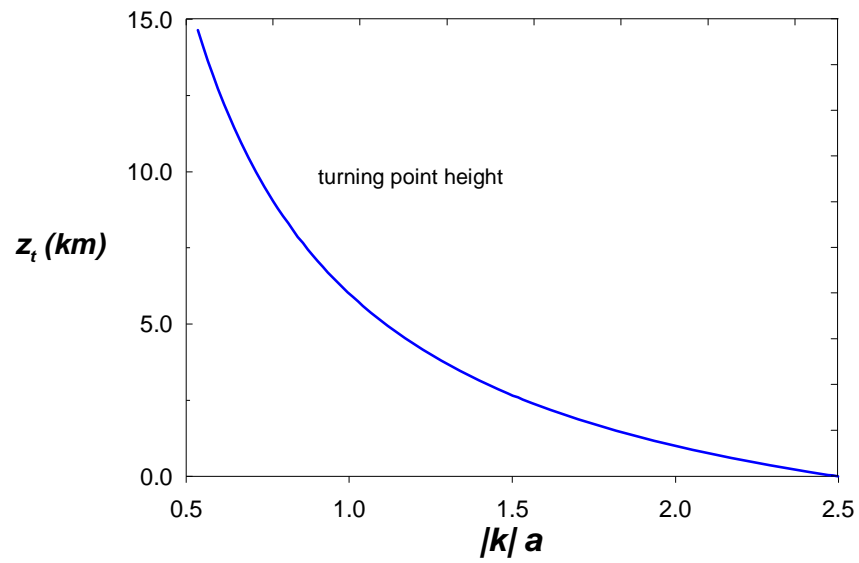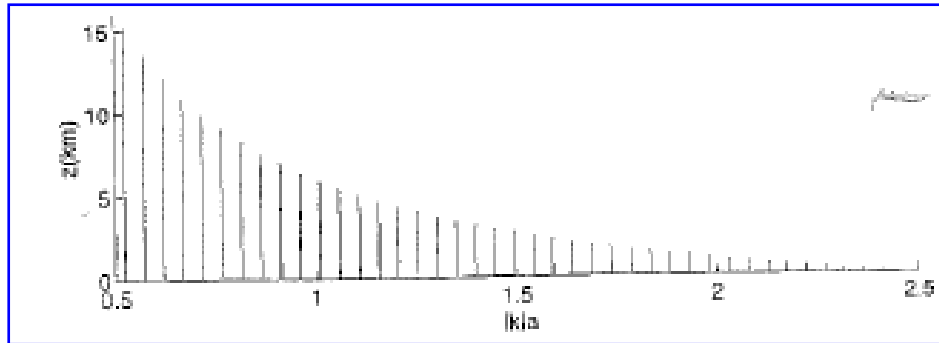
Figure 12. Turning point height z_t as a function of wave number.

Atmospheric specification: (Case II from Wurtele et al, 1987)

$U = U_0 \cdot (1 + z/L)$ $\quad\quad$ $N = 0.01\,s^{-1}$ $\quad$ a = 2500 m $\quad$ h = 100 m

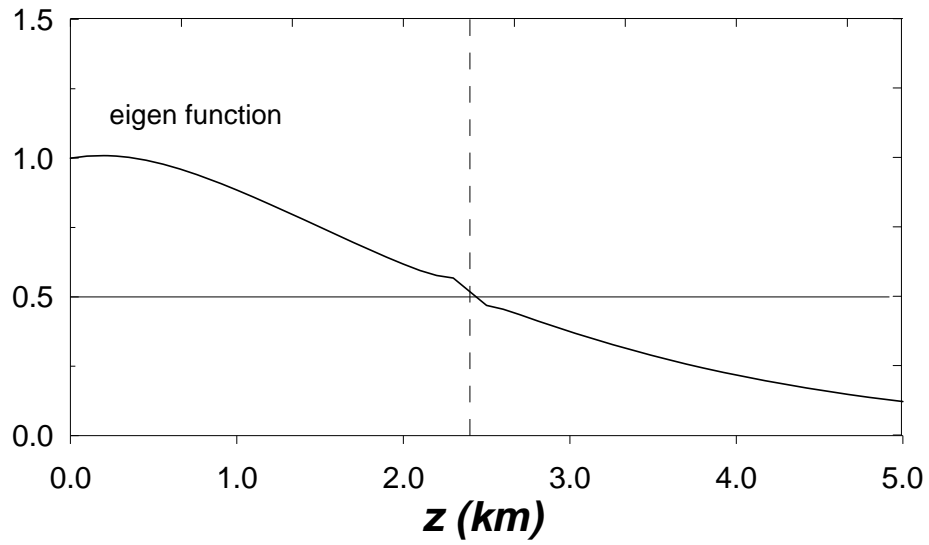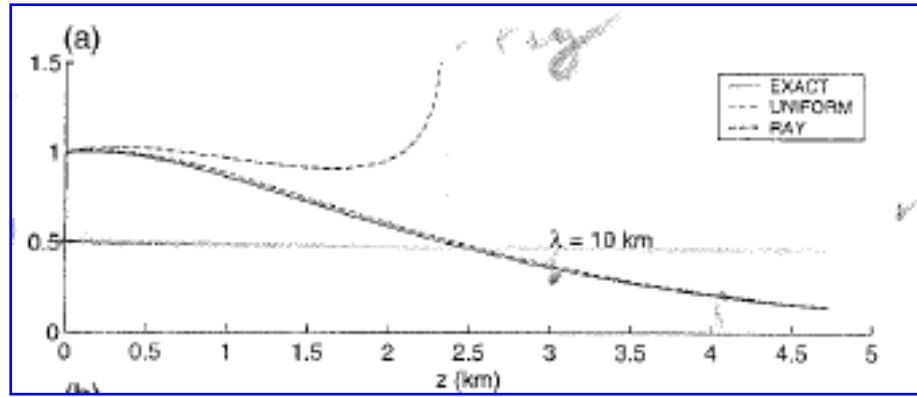$U_0 = 10\,ms^{-1}$; $\ L = 4\,km$ $\quad$ Richardson number = 16

Figure 13a. Comparison of vertical eigenfunction $\mathrm{Re}\left(\tilde{\eta}_u/\tilde{h}\right)$ for λ =10 km as a function of height using MWFM-3 (2-D) for trapped wave modes. Dashed line marks turning point height z_t.
Lower boundary specification: $\tilde{h}(k) = h_0 a e^{-a|k|}$ $h_0 = 100\ m$ (Witch-of-Agnesi)
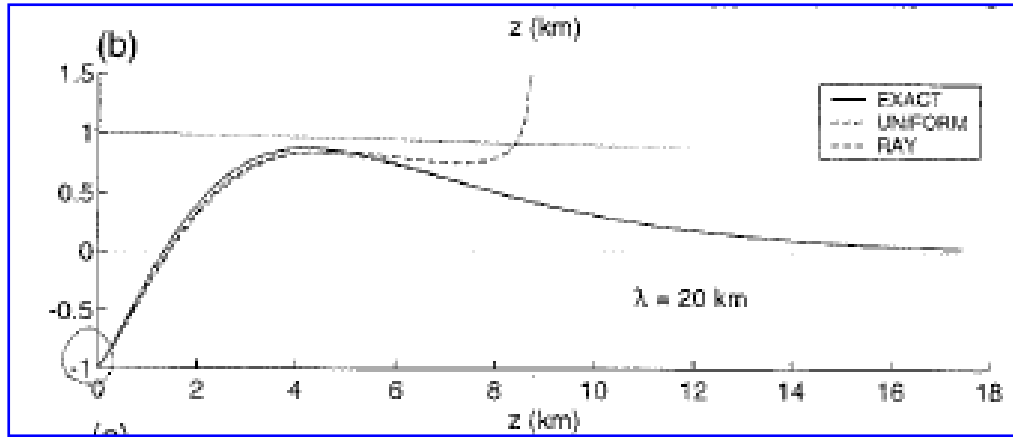Published solution (Broutman et al, 2003) is at top.
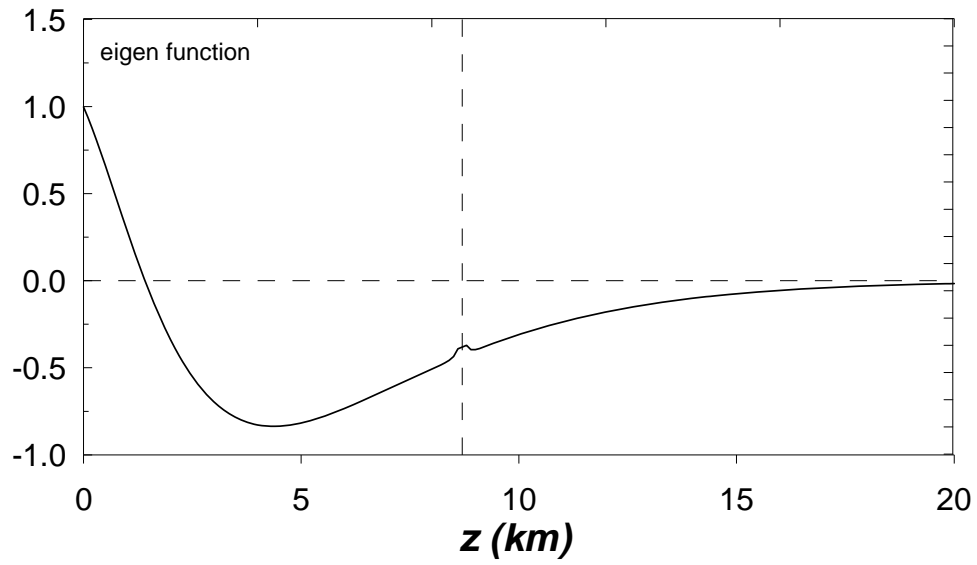
Figure 13b. As in figure 13a, except $\mathrm{Re}\left(\tilde{\eta}_u/\tilde{h}\right)$ for λ=20 km. Vertical dashed line indicates turning point height z_t.
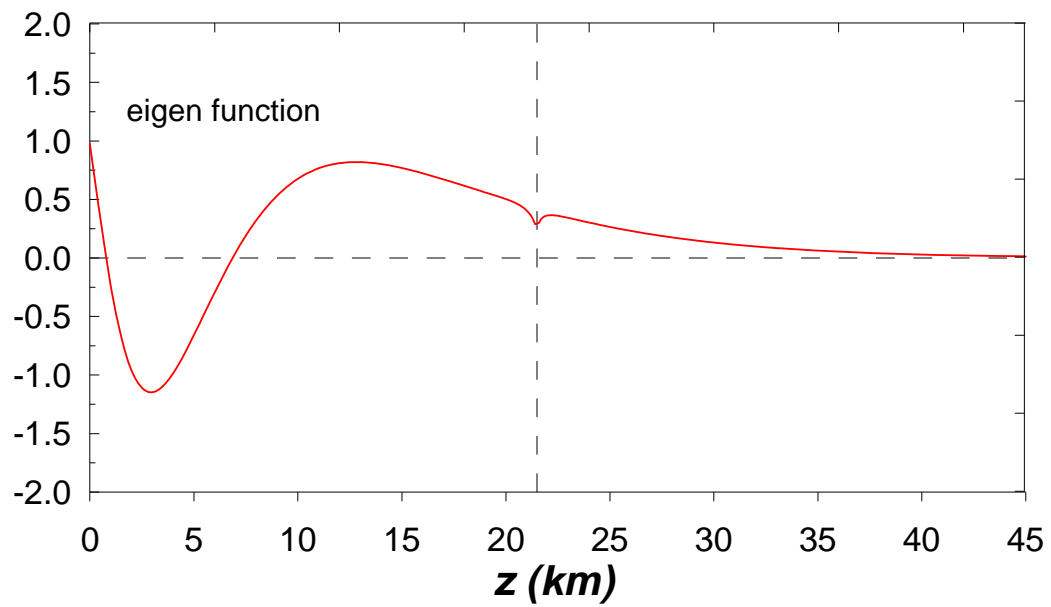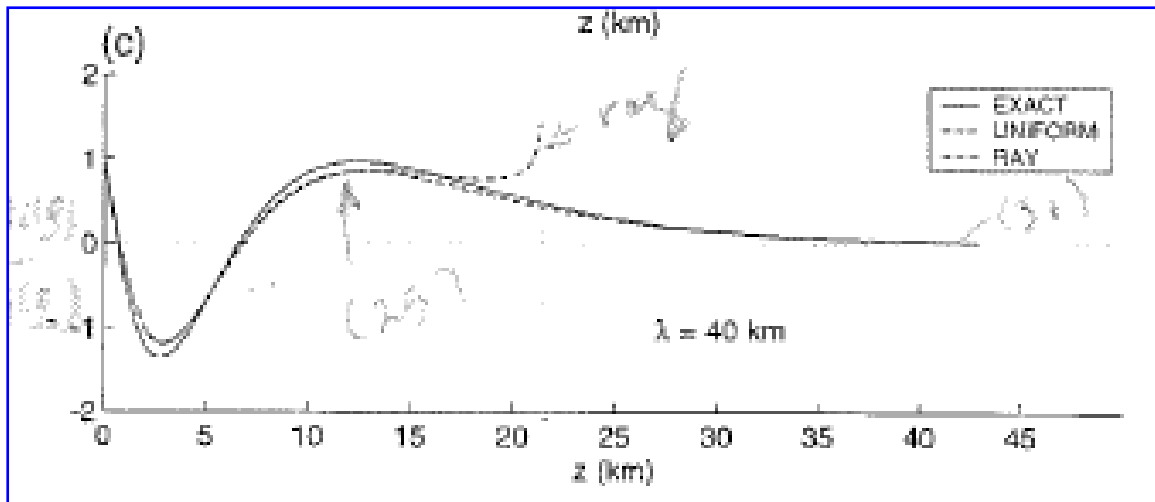
Figure 13c. As in figure 13a but for comparison of vertical eigenfunction $\mathrm{Re}\left(\tilde{\eta}_u/\tilde{h}\right)$ for $\lambda = 40$ km. Vertical dashed line indicates turning point height z_t.
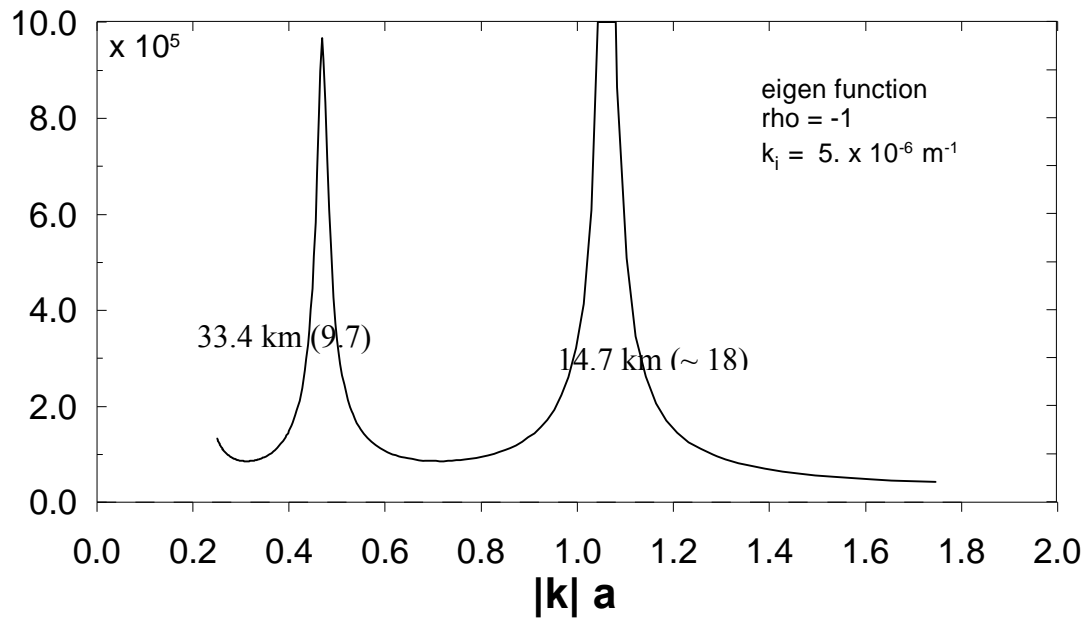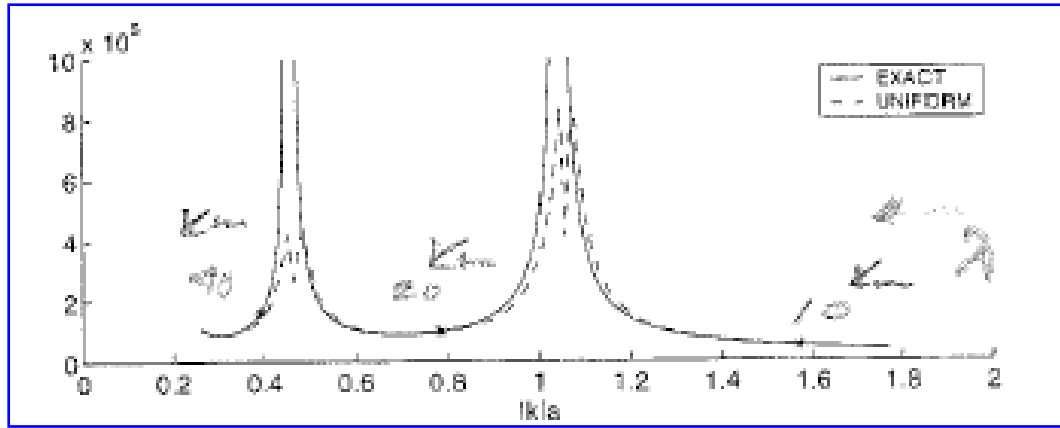
Figure 14. From Broutman et al (2003) representing uniform 2-D MWFM-3 solution $|\tilde{\eta}_u(k)|$ (m^2 rad^{-1}) for $\rho = -1$. Parentheses denote eigenfunction peak magnitude (m^2 / rad$^{1/2}$). Atmospheric and terrain specifications used are as listed in Figures 12 and 13. Published solution is at top.
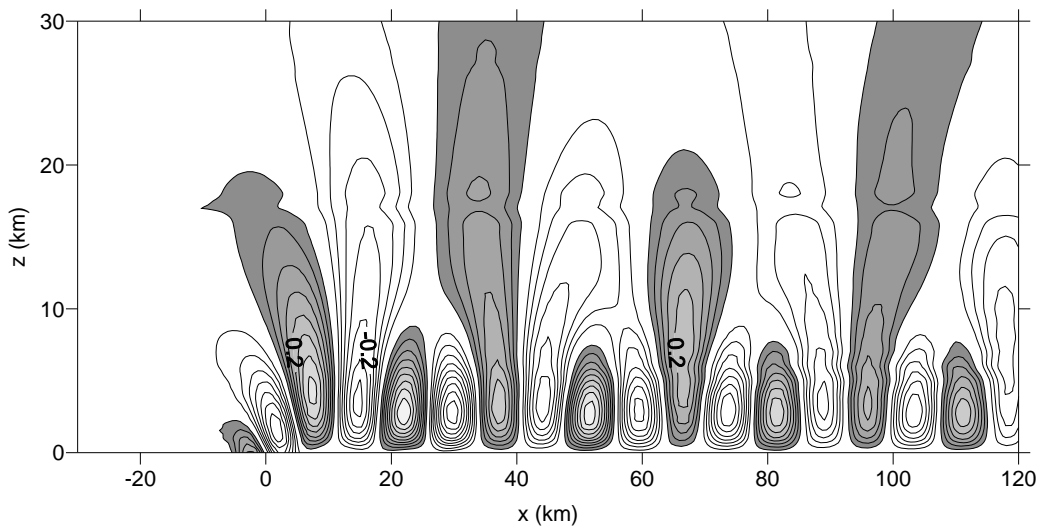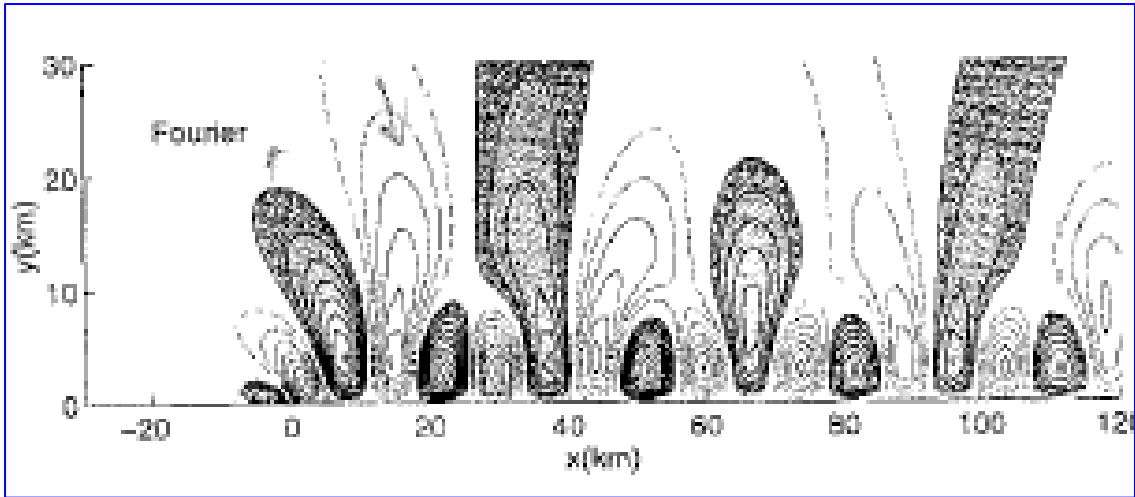
Figure 15. Comparison of two-dimension cross-section for
MWFM-3 steady-state version with trapped waves.

$k_i = 5 \times 10^{-6}$ rad/m $w_{max} = +0.39$ m/s (+0.38)
$s = 1024$ km $w_{min} = -0.39$ m/s (-0.37)
$n = 1024$ $\Delta w = 0.04$ m/s
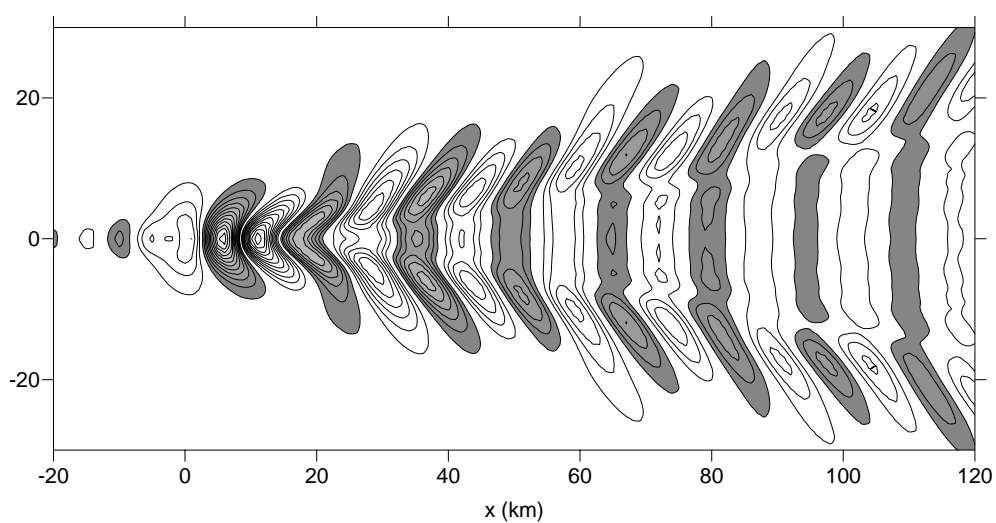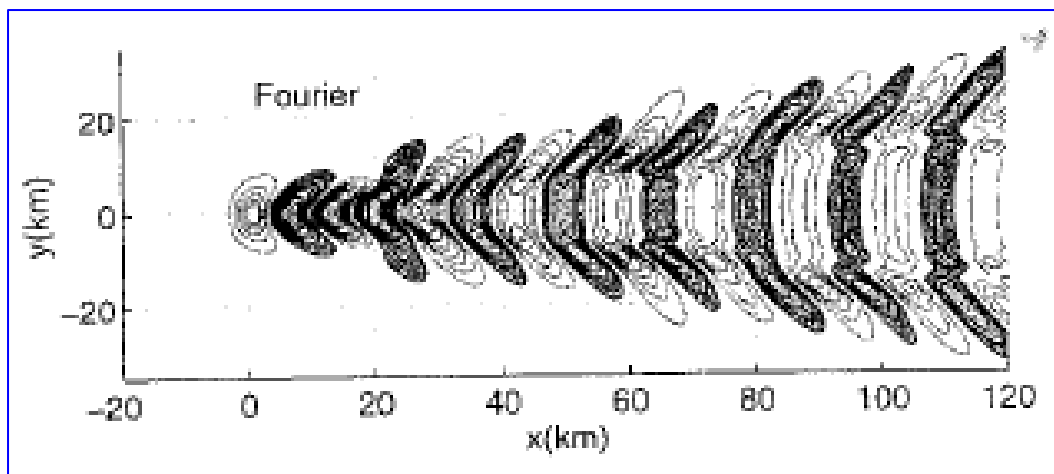$\Delta z = 1$ km

Figure 16. MWFM-3 trapped wave solutions Published value at top
$ki = 5 \times 10^{-6}$ for kx only   same terrain and atmospheric specification as Fig. 13
$s = 1024$ km $z = 2.5$ km
$n = 1024 \times 1024$ $w_{max} = + 0.25$ m/s (+0.21)
                             $w_{min} = - 0.24$ m/s (-0.18)
                             $\Delta w = 0.02$ m/s

argument of the Airy function.   A secondary modification involved evaluation of the phase integrals analytically instead of numerically. The dispersion relation for this case is in a form which permits ready evaluation using integral tables. Once these modifications were accomplished, the results in Figures 15 and 16 matched the published results. This behavior suggests the MWFM-3 results for trapped wave modes can be sensitive to phase function evaluation.

The trapped mode results displayed in Figures 15 and 16 can also be tested and reproduced using a non-linear numerical model given the same initial conditions. In Broutman et al (2003), a nonlinear, Boussinesq, second-order finite difference numerical model is run out to 1.5 hours until a steady-state solution is obtained. It uses a "sponge layer" for x > 80 km and z > 35 km. The results from the nonlinear model and linear model match almost exactly.

6.4   Use of the Airy Function in MWFM-3

MWFM-3 solutions for trapped wave modes require evaluation of the Airy function, also referred to as the Airy integral, for real and/or complex arguments. The Airy integral can be applied in the vicinity of caustics to treat the breakdown of ray wave theory (Lighthill, 1978). Its analytical evaluation procedures are described in Appendix B.   The Airy function $Ai(z)$ can be calculated very accurately using ascending series where $z \equiv x + iy$ is complex. However, the series' relatively slow convergence dictates a much quicker calculation method when potentially millions of evaluations must be repeatedly made.

For parameterization of the Airy function involving only the real argument x, a three-zoned approximation can be used where (1) auxiliary functions are employed toward the extrema, (2) an approximation from Lighthill (1978) is used for significant negative x, and (3) a polynomial fit is used in the vicinity of $x = 0$. Both the ascending series solution and the fast parameterization are plotted in the first figure of Appendix B to illustrate their equivalence.

A machine-oriented algorithm (Amos, 1986) is used for fast calculation of the Airy function with complex arguments. Its evaluation in the complex plane compares well with those obtained using the series expansion, as displayed in the modulus and phase contour charts of figures B2 and B3 in Appendix B.

6.5 Numerical Evaluation of the Phase Integral for MWFM-3:

Implementation of MWFM-3 for use with routine weather data requires the capability to numerically evaluate the phase integrals. Figures 17 and 18 depict plots of vertical velocity (m/s) calculated at 6.3 km using the hydrostatic assumption for the dispersion relation, constant Brunt-Vaisala frequency, and the horizontal wind velocity for two cases -- one where the wind vector is backing with height and one where the zonal wind is constant with height. The lower boundary terrain is a 200 meter bell-shaped hill with a half-width of 20 km (see figure 19). The phase integral is calculated numerically over 64

levels ($\Delta z = 100$ m) using the trapezoidal rule on a 1024 x 1024 horizontal mesh ($\Delta \sim 1$ km) in lieu of an analytical evaluation of the phase integral. Critical levels, where the
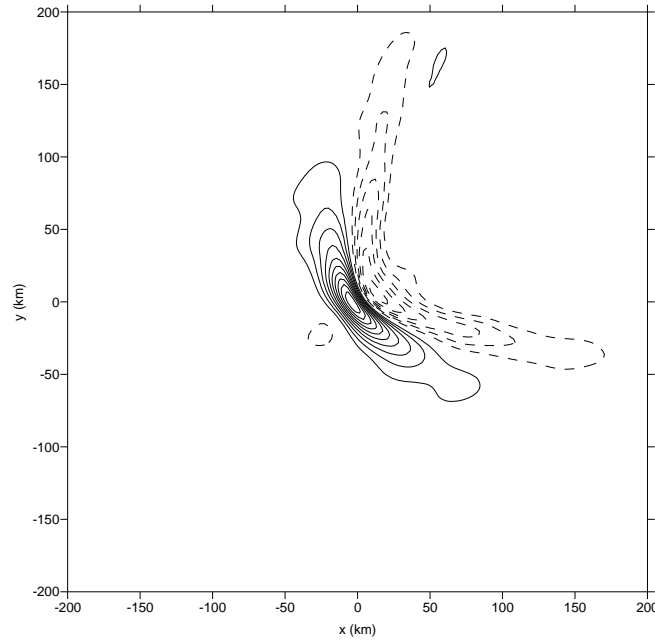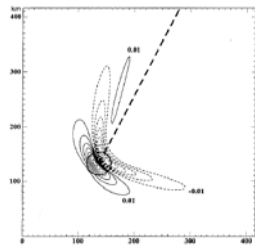

z = 6.3 km MSL, $\Delta z = 100$ m, 64 levels
max vertical velocity = 0.108 m/s
min vertical velocity = - 0.066 m/s
hydrostatic dispersion, wind backing with height
u = +10 m/s, N = 0.01 s^{-1}

$v_0 = 0.$, $\dfrac{dv}{dz} = 0.003$ s^{-1}

$$\hat{\eta}(k_x,k_y,z) = \hat{h}(k_x,k_y,z)\left[\frac{G_0(k_x,k_y,z_0)}{G(k_x,k_y,z)}\right]^{\frac{1}{2}} \exp\left[i\phi_p\right] \quad (\text{m}^3 \text{ rad}^{-1})$$

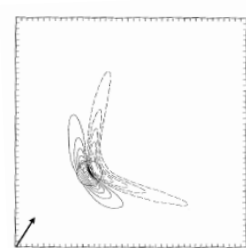$$\phi_p(k_x,k_y) \equiv -\int_0^z m(k_x,k_y,z)dz \quad (\text{rad})$$
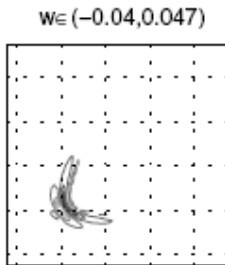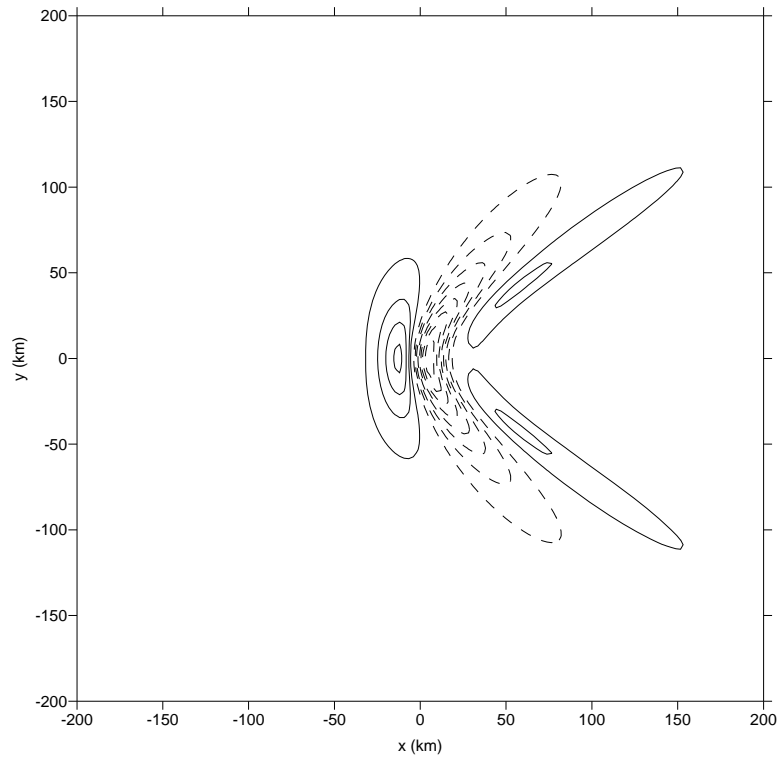

Tanushev et al
(UCLA)

Shutts and Gadian, 1999
(analytical) (+ 0.08, -0.07)

Doyle and Jiang, 2006
(analytical) (+ 0.09, -0.06)

Figure 17. Plot of hydrostatic mountain wave solutions with base state wind backing with height as specified above. Dashed line on the Shutts and Gadian plot shows the wind direction at z = 6.3 km.

z = 6.3 km MSL, Δz = 100 m, 64 levels
max vertical velocity = 0.043 m/s
min vertical velocity = - 0.088 m/s
hydrostatic dispersion, constant zonal wind with height
u = +10 m/s, N = 0.01 s^{-1}
v = 0 m/s
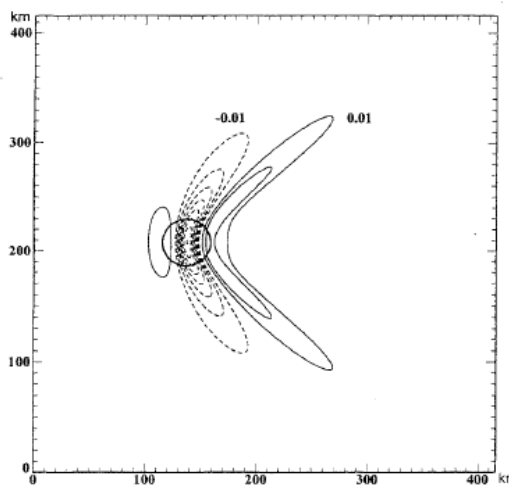
Shutts and Gadian, 1999
analytical (0.03, -0.07)
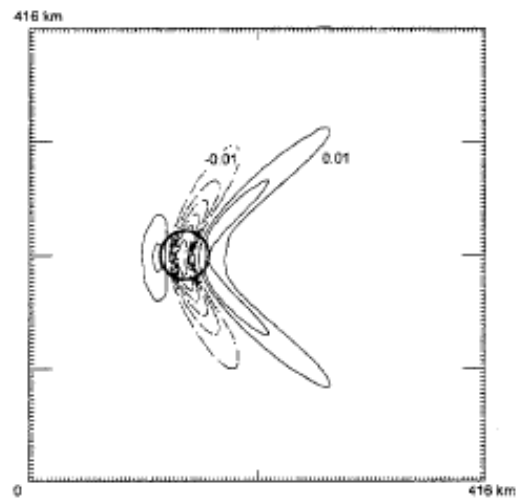
Shutts and Gadian, 1999
numerical model (0.03,-0.065)

Figure 18.   Plot of hydrostatic mountain wave solutions with constant zonal wind with height as specified.

intrinsic frequency is zero, are skipped. 1004 critical levels were detected for the backing wind case out of a total ~ 67 x 10^6 points.

The examples depicted in Figures 17 and 18 were originally published by Shutts and Gadian (1999) but other authors have replicated these examples including Tanushev et al (2007) using the Gaussian beam method and Doyle and Quing (2006) using a modified version of Smith's model. At the bottom of the figures, the calculated results for wind backing with height are compared with their results as well as Shutts and Gadian's non-hydrostatic numerical simulations and hydrostatic analytical solutions. The maximum and minimum vertical velocities obtained by the different investigators generally agree.
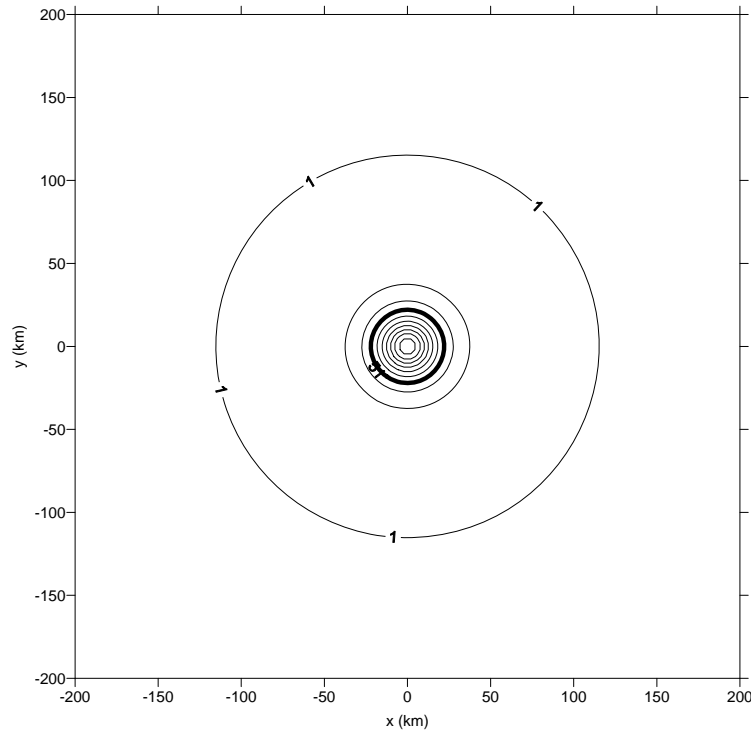
Fig. 19   Bell-shaped terrain used in model calculations (meters), for figures 17 and 18, with 200 meter height and 20 km half-width. Inner contour intervals are approximately 20 meters.

6.6   MWFM-3: Discrete, Steady-State, Linear, Hydrostatic and Non-hydrostatic

Broutman's linear steady-state MWFM-3 model for hydrostatic and non-hydrostatic solutions can be expressed in fully discrete form. The distinguishing features between this and results presented above are the provisions for (1) discrete, multi-level input for the basic state, such as provided by rawinsonde or numerical models, including the digitized terrain data base, and (2) a switch for calculating hydrostatic or non-hydrostatic solutions including trapped wave modes.
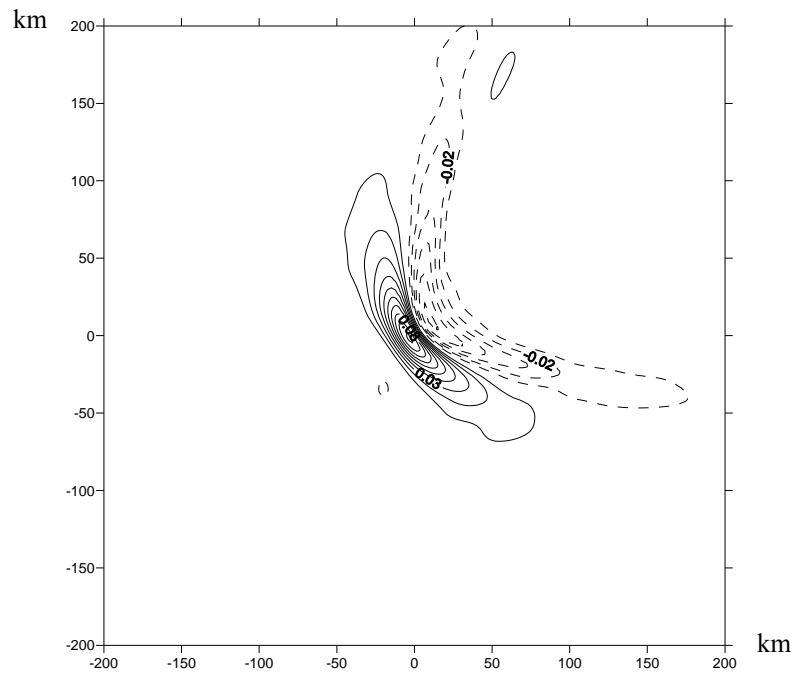
$w_{max} = +.102383$, $w_{min} = -0.062303$ $z = 6.3$ km
$h_m = 200$ m ; Gaussian hill ½ width = 20 km
$N = 0.01$ s^{-1}, $U = 10$ m/s
$V_{sfc} = 0$, $dv/dz = 3 \times 10^{-3}$ s^{-1}
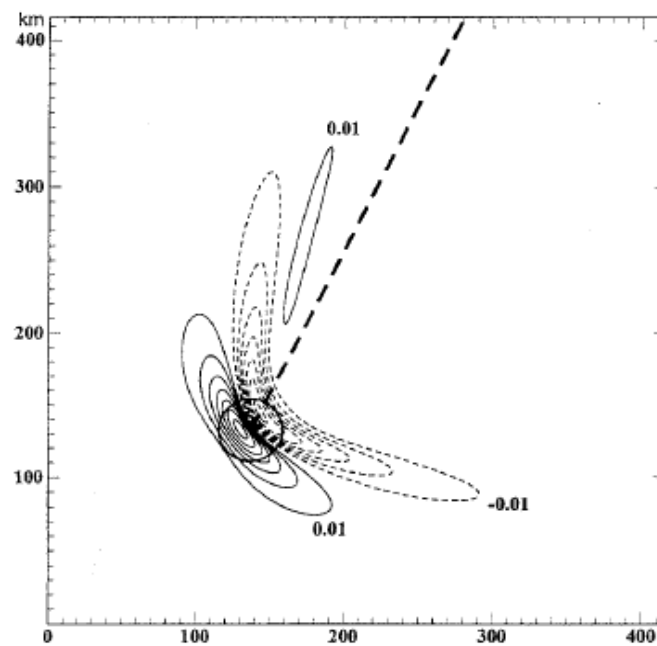
Shutts and Gadian, 1999
(analytical) (+ 0.08, -0.07)

Figure 20. Hydrostatic (wind backing with height) . Fully Discrete version
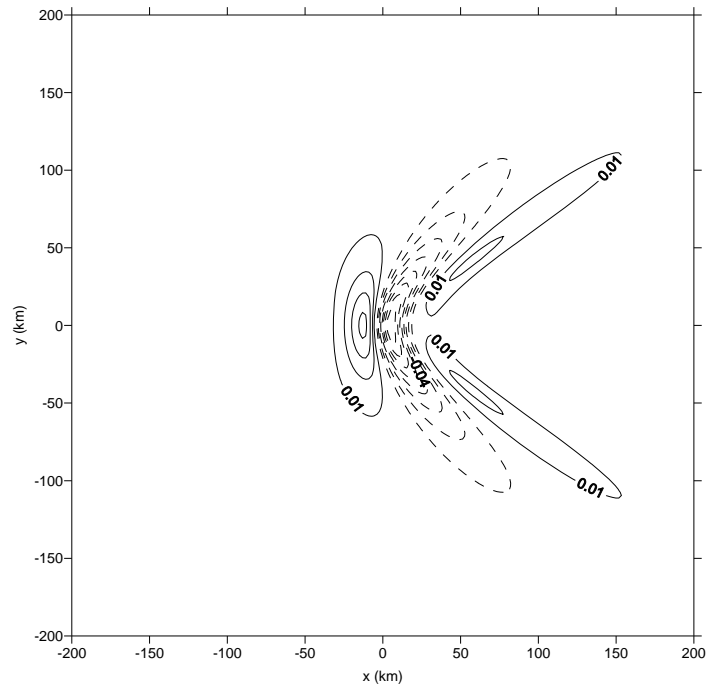
trapezoidal rule, hydrostatic dispersion
$w_{max} = +0.043$, $w_{min} = -0.088$ m/s $z = 6.3$ km
$h_m = 200$ m ; Gaussian hill ½ width $= 20$ km
$N = 0.01$ s^{-1}, $U = 10$ m/s , $V = 0$
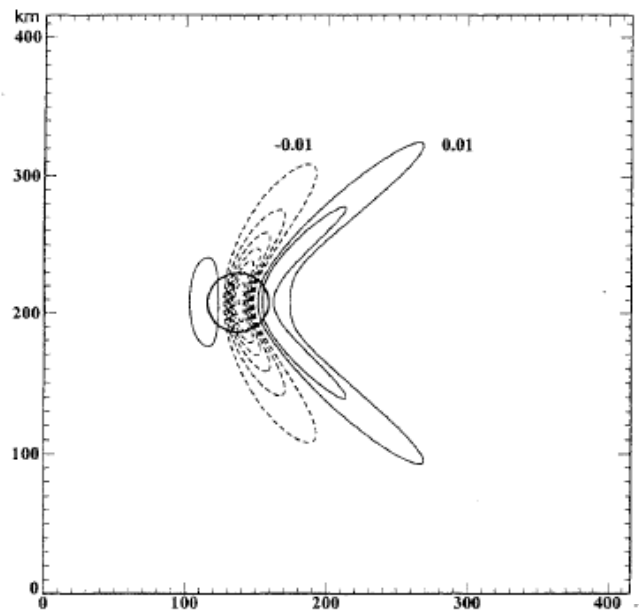
Shutts and Gadian, 1999
analytical (+ 0.03, - 0.07)

Figure 21.   Hydrostatic (zonal wind constant with height) Fully Discrete version
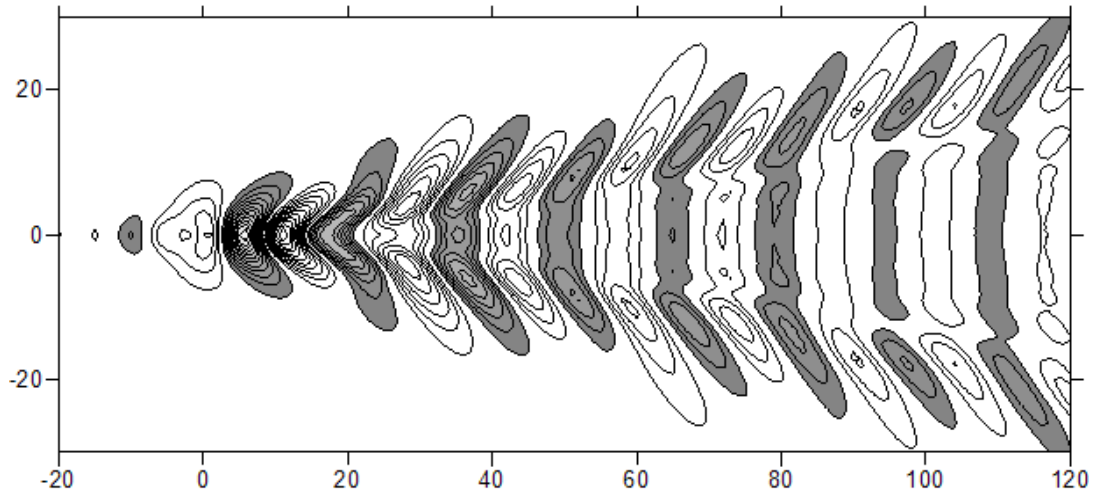
$w_{max} = +0.25$ m/s , $w_{min} = -0.24$ m/s
contour interval $= 0.02$ m/s $h_{max} = 100$ m $\lambda_{res} \sim 15$ km
Gaussian half-width $= 2.5$ km , $z = 2.5$ km
sfc: $U_0 = 10$ m/s $dU/dz = 10/4000$ s^{-1} $N = 0.01$ s^{-1}

$w_{maz} = +0.21$ m/s, $w_{min} = -0.18$ m/s , $\lambda_{res} \sim 15$ km
analytical inputs for shear, stability, turning points (Broutman et al, 2003)
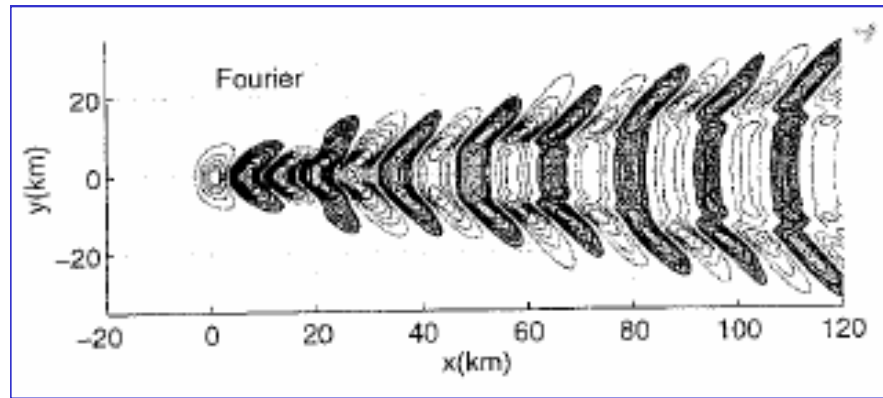
$w_{max} = +0.25$ m/s, $w_{min} = -0.21$ m/s (Broutman et al, 2003)
non-linear, Boussinesq, free-slip lower boundary, sponge layer for $x > 80$ km
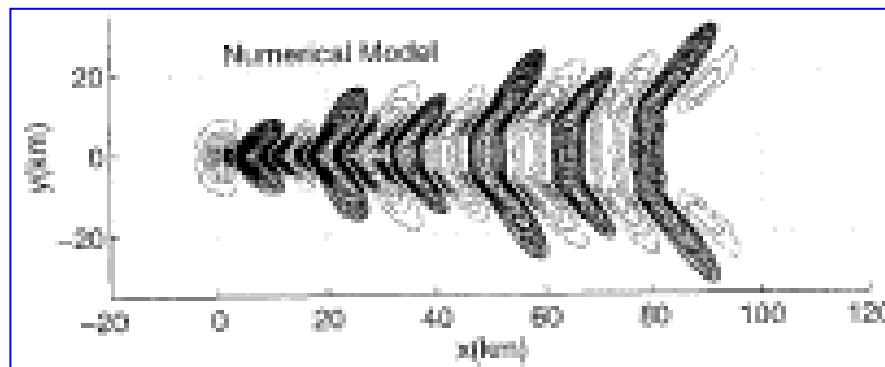
Figure 22. Non-hydrostatic (constant wind shear with height; fixed static stability) Fully discrete

Analytical functions and dependencies involving the basic state (wind velocity and temperature) and phase behavior are removed. A two-dimensional lower boundary is defined in real space and then transformed. Phase integrals are evaluated numerically using the trapezoidal rule. The existence of turning points and critical levels are checked for and determined objectively at each level for all wave numbers. An upper altitude limit of 30 km is imposed for turning point checks, consistent with the upper limit of typical NWP and rawinsonde data. Altitude increments can vary within the vertical column. For the examples here, a uniform height increment of 100 m is used.

These particular examples employ numerically-determined turning points and numerically-evaluated phase integrals for hydrostatic (Figures 20 and 21) and non-hydrostatic trapped wave test case (Figure 22) using Broutman's steady-state model (Broutman et al, 2003). For evaluation purposes, a turning point exists when the real part of the vertical wave number (dispersion relation) changes sign between levels, or its modulus is zero at a level. Critical levels, where the intrinsic frequency is zero, and "zero altitude" turning points, are skipped for the Fourier transform evaluation.

Comparisons of MWFM-3 steady-state discrete solutions (in the upper figure half) with published results (in the lower half) are shown for the hydrostatic and non-hydrostatic cases. Solutions for vertical velocity are calculated on a 1024 x 1024 horizontal mesh using a mesh spacing of 1 km. Wind profiles are treated effectively as continuous functions using constant values of speed or shear with height. Stability values can also be allowed to change abruptly between levels for the non-hydrostatic model comparisons. However, such a stability profile behavior may not always be appropriate for a multi-level discrete approach.

One deficiency in the MWFM-3 formulation as published is the neglect of boundary layer wave absorption associated with the surface stagnant layer, as in the manner discussed by Smith et al (2002).

7. TRANSIENT WAVE SOLUTIONS (MWFM-3):
   (Broutman et al, 2006)

The general transient or time-dependent trapped wave solution for $\tilde{\eta}_{tr}$, described in Broutman et al (2006), is:

$$\tilde{\eta}_{tr} = \tilde{\eta}_u + \left(M_1 - M_2\right)\tilde{h}\left[G_0/G\right]^{\frac{1}{2}} e^{i(\phi + M_2\Phi)} = \tilde{\eta}_{tr}\left(k_x, k_y, z, t\right) \quad (\text{m}^3\,\text{rad}^{-2}) \tag{21}$$

where $\quad \tilde{\eta}_u = 2i\pi^{\frac{1}{2}}(-r)^{\frac{1}{4}} A \cdot \text{Ai}(r) e^{i\left(\xi - \frac{\pi}{4}\right)} S_{M_2}$ $\tag{22}$

$\quad A = \tilde{h}\left[G_0/G\right]^{\frac{1}{2}}$ (wave action density), M_1 and M_2 are the trapped wave counters

$\quad G = \rho N^2 c_g / \sigma$ (kg m^{-2} s^{-2} rad^{-1}), ρ here being air density (kg/m^3)

$\quad Ai(r)$ is the Airy function for the argument r

$\quad \tilde{h}\left(k_x, k_y\right)$ represents the topography of the lower boundary in the wave number

$\quad$ domain. For a bell-shaped hill, $\tilde{h}(k_x, k_y) = h_0 a^2 e^{-a(k_x^2 + k_y^2)^{\frac{1}{2}}}$

$$S_{M_2} = \frac{1 - e^{iM_2\Phi}}{1 - e^{i\Phi}} \equiv 0 \text{ if } M_2 = 0$$ is the summation expression for trapped waves. The time-dependent trapped wave behavior and related nomenclature are discussed further below. The group velocity is, as described earlier in Eq. (17),

$$c_g = \frac{\partial \sigma}{\partial m} = -\left(k_x^2 + k_y^2\right)^{1/2} \cdot N(z) \cdot m(z) \Big/ \left(k_x^2 + k_y^2 + m(z)^2\right)^{3/2}.$$

For the lower boundary condition, the height field perturbation is set equivalent to the topography, or $\tilde{\eta}(k_x, k_y, 0) = \tilde{h}(k_x, k_y)$. The Airy function argument r is complex. In the transient model implementation, however, both $Ai(r)$ and its argument r are treated as real functions.

The phase relations for the transient wave solution are similar to those for the steady-state solution. For the vertically propagating waves,

$$\phi(k_x, k_y, z) \equiv -\int_0^z m(k_x, k_y, z) dz \quad \text{(radians)} \tag{23}$$

For the trapped waves,

let $\Phi = 2\hat{\phi} - \pi/2$, where $\hat{\phi} = -\int_0^{z_t} m\, dz$; and $\xi = \frac{1}{2}(\phi_1 + \phi_2)$, $r = -\left[\frac{3}{4}(\phi_1 - \phi_2)\right]^{2/3}$

If $z_t < z$ where z is the level of analysis, then the expression for r will have a positive sign. If $z_t = z$, then $r = 0$.

Let ϕ_2 represent the phase for waves reflected from the caustic and ϕ_1 represent the phase for waves incident upon the caustic. These phase functions are defined as:

$\phi_2 = \hat{\phi} - \int_z^{z_t} m\, dz = -\int_0^{z_t} m\, dz - \int_z^{z_t} m\, dz$ (radians), the phase for waves reflected from the caustic, and

$\phi_1 = -\int_0^z m\, dz$, the phase for waves incident upon or below the caustic

z is the analysis level, and z_t is the turning point height (m), that is, the height where the vertical wave number m becomes less than or equal to zero.

The relevant wave dispersion relations for the transient trapped solutions are the same as the non-hydrostatic steady-state formulation:

$$m = k_h \left[\frac{N^2 - \sigma^2}{\sigma^2}\right]^{1/2} \text{ (rad/m)} \; ; \; \sigma = -k_x \bar{U} - k_y \bar{V} \text{ (rad s}^{-1}\text{)} \; ; \; k_h = \left(k_x^2 + k_y^2\right)^{1/2} \text{ (rad m}^{-1}\text{)} \tag{24}$$

and $\quad \tilde{h}(k_x, k_y) = \frac{1}{2\pi} \int_{-\infty}^{\infty} \int_{-\infty}^{\infty} h(x, y) e^{ik_x x} e^{ik_y y} dx\, dy \text{ (m}^3 \text{ rad}^{-1}\text{)} \tag{25}$

For the example described below in section 7.2, $\bar{U}(z) = U_0(1 + z/L) \text{ (m s}^{-1}\text{)}$

According to Broutman et al (2006), no imaginary component need be added to the horizontal wave number k_h for the transient solution to produce damping at resonant frequencies.

7.1 Illustration of time-dependent trapped wave behavior

The diagram below (Figure 23) illustrates schematically the time-dependent trapped wave behavior at a single wave number. Given time t *(sec)*, $M_1 = M_2 = \text{round}(t/2T)$ where the propagation time T from the ground to the turning point is: $T = m_0 L / k_x U_0$ (sec) and M, an integer function of time, is the trapped wave round-trip counter. In Figure 23, z_a is the desired analysis level and the "0" subscripts denote surface values. The hatched region depicts the region between the analysis level and trapping level or turning point at z_t, and t_{fr} is the time elapsed for the wave in the present trapped wave cycle.
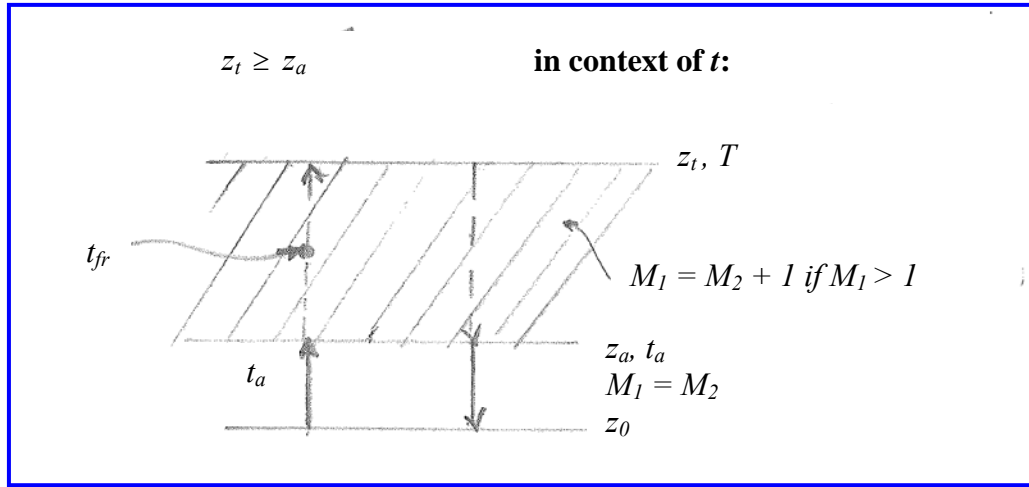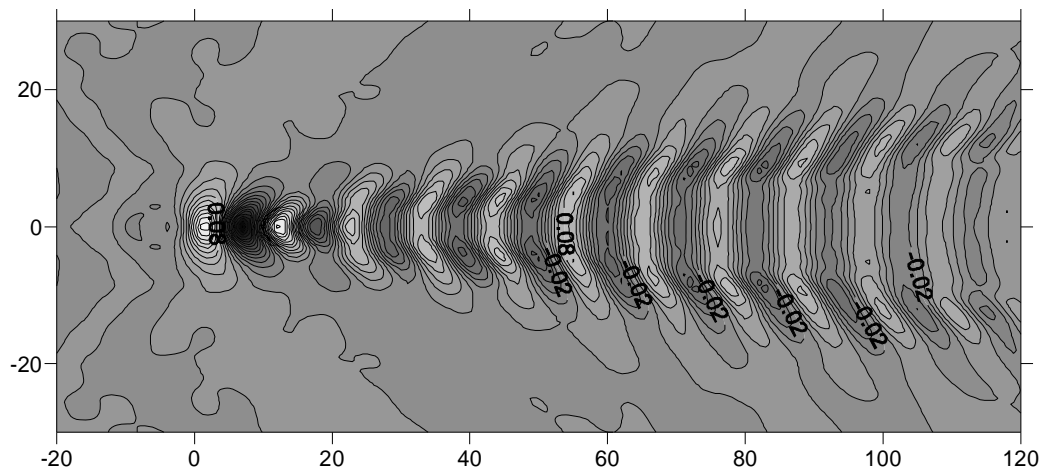

Fig. 23. The time-dependent trapped wave domain for a single mode

If ($z_a < z_t$) and $M_1 = 0$, the trapped wave influence is not included and $\tilde{\eta}_{tr} = 0$. Now, $M_1 = M_2 + 1$ if the wave front lies within the hatched zone, that is, if the wave front is crossing z_a on its way up to the turning point or if it has been reflected from the turning point prior to reaching z_a on its way down. It is important that the round-trip counter for the trapped waves, M_2, be incremented after each round trip. Like the steady-state solution, the MWFM-3 transient solution only accounts for a single turning point in the vertical column for each wave number mode.

7.2 Discussion of results for MWFM-3 transient model comparison:

Calculations displayed in Figures 24, 25, and 26 are compared with Broutman et al's (2006) example results for their Fourier-ray solutions. The input parameters, like those used in Figures 16 and 22, are $L = 2.5$ km for the linear zonal wind shear profile definition, $a = 2.5$ km for the bell-shaped hill radius, $h_0 = 100$ m for the hill peak, $N = 0.01$ s^{-1}, and a surface wind speed of $U_0 = 10$ m s^{-1}. Calculations were performed on a 1024 x 1024 horizontal grid with approximately 1 km grid spacing. Calculations used to construct the vertical cross-sections were performed at 1 km vertical intervals. Broutman et al (2006) also obtained results similar to those of MWFM-3 using a numerical model

setting: $\phi_1 = -\int_0^z m\,dz$; $\phi_2 \neq 0$ for z > zt

$\eta_p \neq 0$; Airy function and its argument are real

$w_{max} \sim +0.21$, $w_{min} \sim -.30$ m/s
contour interval is 0.02 m/s

$w_{max} \sim +0.23$ m/s

t = 3 hrs

From Broutman et al, 2006. contour interval is 0.025 m s^{-1}

Figure 24. Comparison of vertical velocities calculated at z = 2.5 km, t = 3 hours for MWFM-3 transient solution
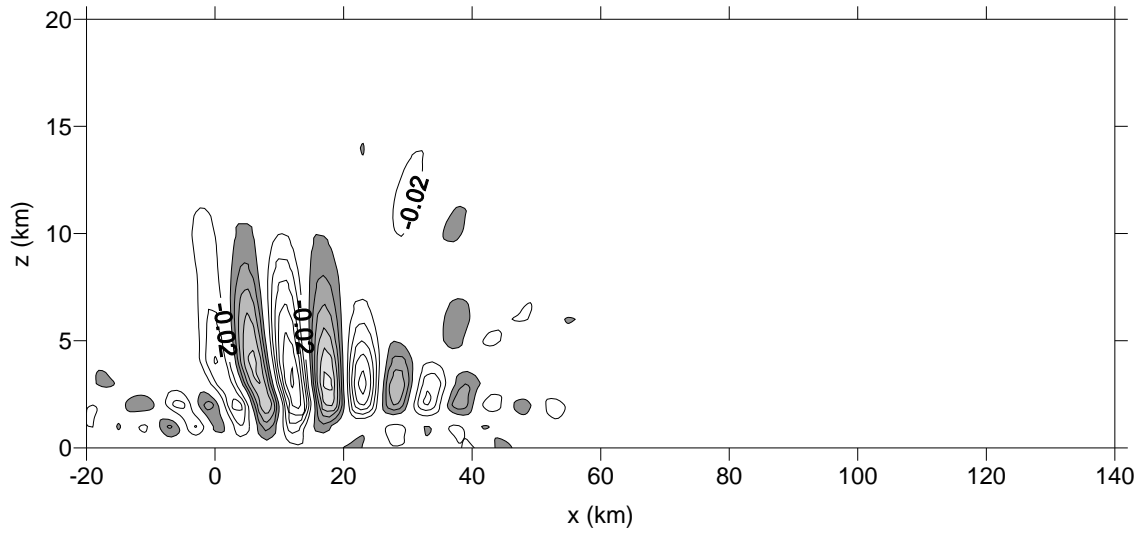
setting: $\phi_1 = -\int_0^z mdz$; $\phi_2 \neq 0$ for z > zt

$\eta_p \neq 0$; Airy function and its argument are real

density scales vertically with scale height = 10 km

time = 1 hour contour interval = 0.025 m/s

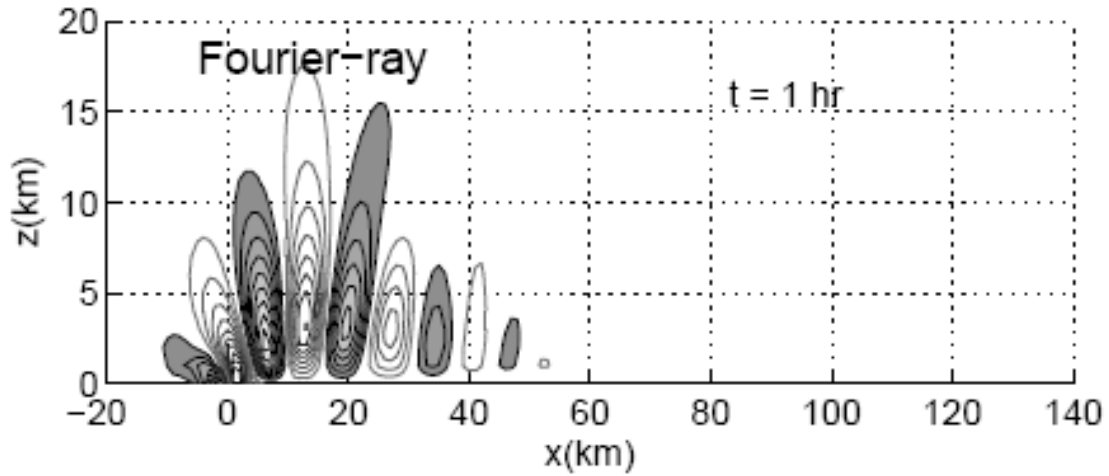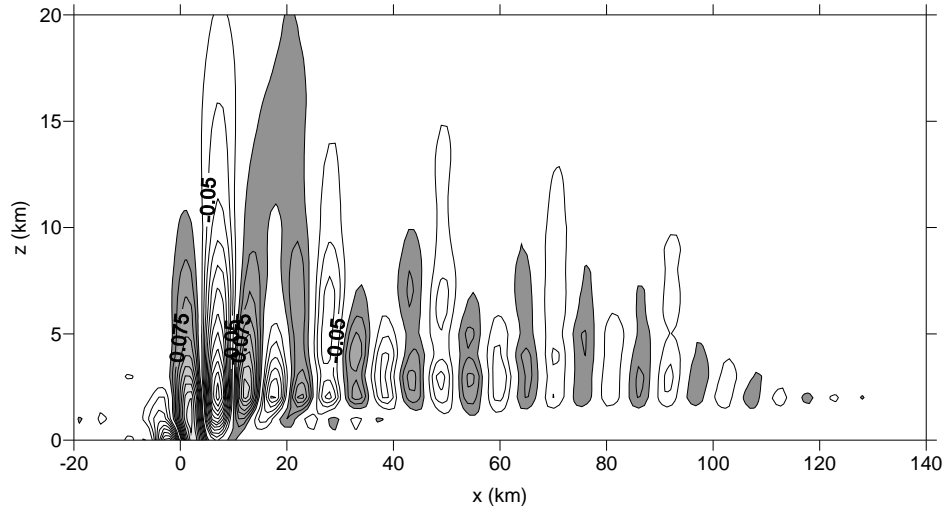Figure 25. East-west vertical cross-section of vertical velocities along hill latitudinal center line (y = 0) for MWFM-3 transient solution at t = 1 hour.

setting: $\phi_1 = -\int_0^z m\,dz$; $\phi_2 \neq 0$ for z > zt

$\eta_p \neq 0$; Airy function and its argument are real

at 10 km: +0.066 -0.090 (w m/s)
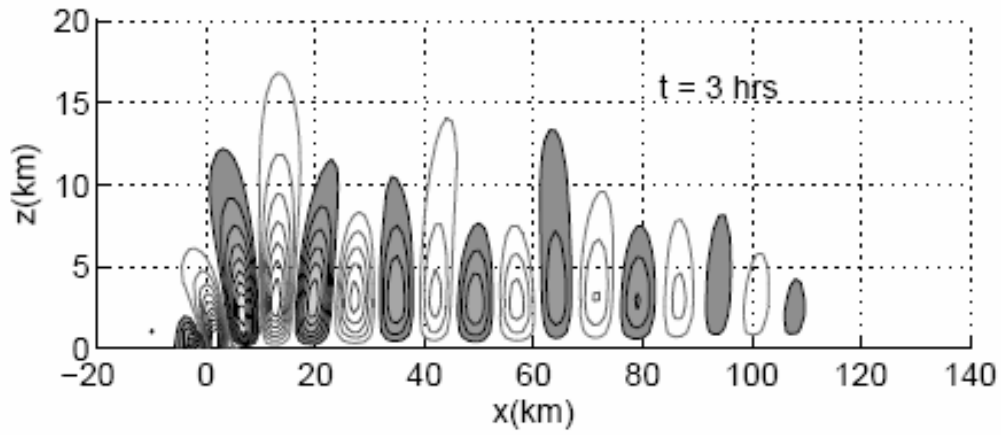at 20 km: +0.027 -0.027 (w m/s)

time = 3 hours

Figure 26. Same as figure 25 but for $t = 3$ hours.

akin to the one developed by Lipps and Hemler (1982). The numerical model had an absorbing sponge near its top and lateral boundaries.

At $z = 2.5$ km for the horizontal plan view (Figure 24) at $t = 3$ hours, the calculated vertical velocity magnitudes ($\sim + 0.21$ /- 0.30 m/s) agree relatively well with the article's Fourier ($+0.23$, -0.19 m/s), and numerical model results ($+0.25$, -0.21 m/s) (which are not shown), respectively. The time-dependent behavior pattern agrees qualitatively with the published figures. However, the calculated trapped mode wavelength (~ 11 km) is significantly shorter than the article figures' wavelength (~ 15 km). Figures 25 and 26 depict the vertical velocity as a function of altitude and distance downstream from the hill location for latitude $y = 0$ at two different times: $t = 1$ hour and $t = 3$ hours, respectively. The zonal vertical cross-section results, compared with the published values (Broutman et al, 2006), also exhibit a shorter wavelength.

Initially, a problem was encountered with the vertical structure of the eigenfunctions. Unless a small imaginary component ($\sim 5 \times 10^{-7}$ radian/m) was added to the horizontal wave number for the x-direction k_x, the eigenfunctions did not damp with height above 10 km. Furthermore, when the imaginary wave number component was included, the peak magnitudes dropped to $\sim 50\%$ of the non-damped amplitudes. This problem was overcome by defining the ϕ_1 component in terms of the vertical integral up to the analysis level and allowing the ϕ_2 phase component always to be non-zero (see Eq. 23 and the following forms). The appropriate procedure for handling the phase functions was not clear from the literature and was discovered after some trial and error.

These results, as was the case for the uniform steady-state solutions, appear sensitive to the phase functions or vertical integrals. The phase function ϕ_1 is not defined explicitly in the journal article (Broutman et al, 2006) and is referred to alternately, in other papers, as the phase integral for vertically propagating waves or as the phase for a ray incident upon the caustic. The source of figure discrepancies may be due, in part, to lack of knowledge of the precise definition of the phase function ϕ_1.

8. APPLICATION OF MWFM-3

The Hawaii 12 December 2002 case used previously to compare Smith's Three Layer model results with balloon-based measurements of vertical velocity is also used to demonstrate the behavior of the MWFM-3 model for a specific application. In Figure 27, the top two plots illustrate the MWFM-3 steady-state, fully discrete, hydrostatic solutions at altitudes of 5 km and 10 km above sea level using the padded Hawaii terrain associated with Figure 7a. and background wind and temperature fields similar to the basic state listed in Table 3. The arrows on the plots depict the horizontal wind direction at altitude. The plots are centered at the same location as depicted in Figure 7a. The resultant MWFM-3 model vertical velocities range from $+ 6.3$ m/s to $- 4.3$ m/s at 5 km. The major axis of the vertical velocity fields or bands is roughly perpendicular to the wind direction at 5 km. At 10 km, the MWFM-3 vertical velocities are noticeably weaker with a range of $+ 1.6$ m/s to $- 1.8$ m/s. Also, the major axis of some vertical velocity bands is approximately parallel to the flow direction at 10 km.
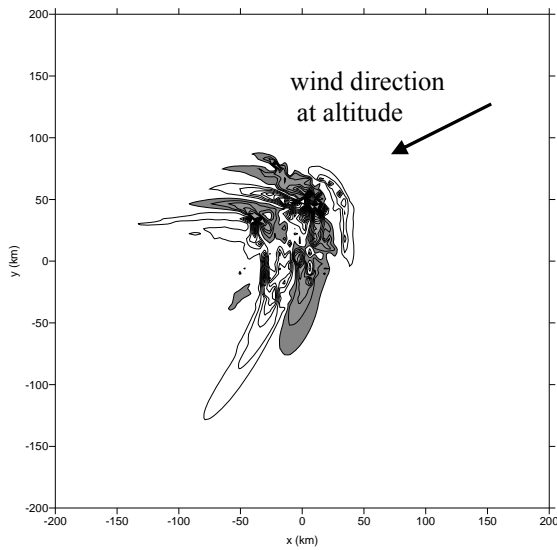
z = 5 km MSL (hydrostatic)
w_{max} = + 6.3 m/s, Δw = 0.2 m/s
w_{min} = - 4.3 m/s (+ w contours dark)
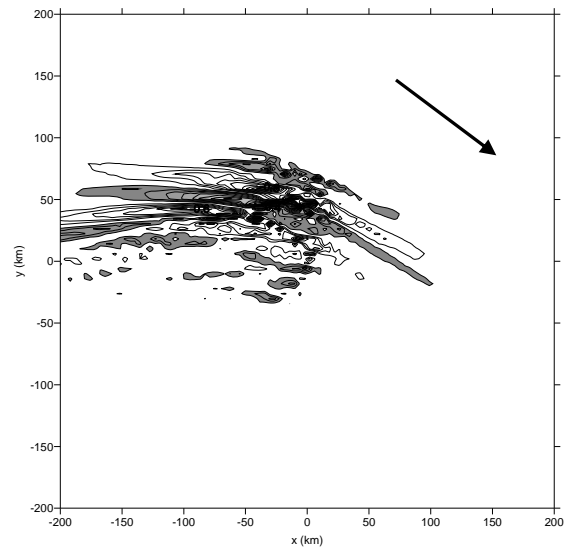
z = 10 km MSL (hydrostatic)
w_{max} = + 1.6 m/s, Δw = 0.1 m/s
w_{min} = - 1.8 m/s (+ w contours dark)
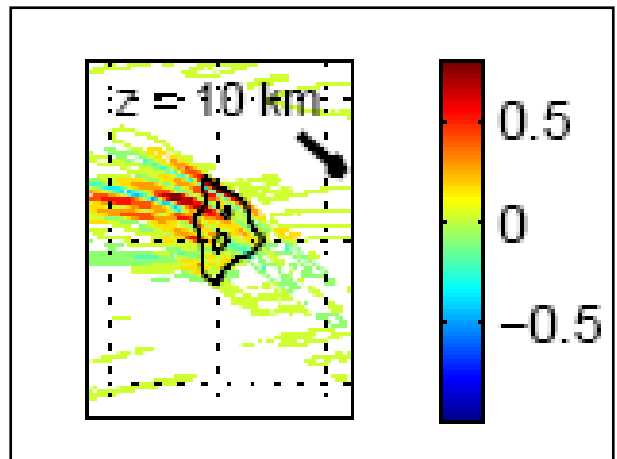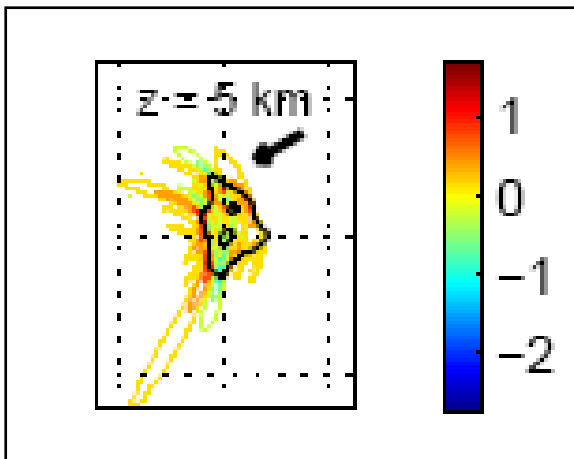
Broutman's transient solution for 12 Dec 2002 100 UTC (grid line spacing = 200 km)
(personal communication, 2007)

Figure 27.   MWFM-3 results using "real-world" Hawaii terrain and atmosphere for 12 Dec 2002
The basic state for the upper plots is taken from GFS data valid at 12 Dec 0600 UTC while the lower
plots use wind and temperature data from Hilo rawinsonde launch at 12 Dec 1200 UTC.

Dr. Broutman (personal communication, 2007) applied the transient wave MWFM-3 model for altitudes up to 18 km for the same location using the Hilo, Hawaii 1200 UTC rawinsonde for the background velocity and temperature profile.   Transient wave solutions for the 5 and 10 km levels, corresponding to the steady-state solutions described above, are depicted in the lower two plots of figure 27.   The spatial distributions of the steady-state MWFM-3 vertical velocity solutions (upper panel) are similar to the transient wave solutions depicted in the lower panels using the Hilo rawinsonde. Differences in lower boundary terrain and background state specification may contribute to the differences in vertical velocity magnitudes between the two MWFM-3 versions.

9. RECOMMENDATIONS

The application of Fourier transforms to practical physical problems has become more routine with the advent of modern small computers. The mountain wave models, Smith Three-Layer, and Broutman MWFM-3, are based on a strong theoretical foundation which has been developed over many years. This foundation is well documented in the literature.   Both Smith Three-Layer and Broutman MWFM-3 have undergone limited verification using aircraft and satellite data (Smith et al, 2002 ; Eckermann et al, 2006). These models are worthy of testing in an operational prediction environment, while remaining cognizant of their physical limitations.

Recently, the Navy has modified the Smith model so that it can be applied to multiple layers, and allows both critical layers and turning of the wind using arbitrary two-dimensional terrain fields for the lower boundary. The modified model is run using operational data at the Naval Research Laboratory (Doyle and Jiang, 2006) for regions such as the Sierra Nevadas and Rocky Mountains and for altitudes up to 12 km above sea level.   The Smith Three-Layer model has not been employed toward prediction of waves in the stratosphere above 15 km.

The Broutman MWFM-3 model, as described, has been developed to include tropospheric and stratospheric wave propagation. It has no theoretical limitations on the number of model levels or the top height. The model results in the literature were typically displayed to 30 km above sea level. This high altitude characteristic favors MWFM-3 testing in an operational stratospheric forecast environment.

The Air Force Weather Agency (AFWA) can implement MWFM-3 in experimental form in regional windows using operational NWP model data for the background states. Implementation details can be provided by Dr. Broutman to numerical modelers at AFWA. Dr. Broutman can advise AFWA modelers on how best to apply the MWFM-3 model. MWFM-3 model output, based on operational forecast models, can be posted on the Joint Air Force & Army Weather Information Network and compared with other experimental mountain wave forecast models including MWFM-2 (Marks and Eckermann, 1995) and the S-Layer Turbulence Model (Sinclair and Kuhn, 1991). MWFM-3 model output can also be verified using stratospheric in-flight observations as they become available.

References

Amos, D.E., 1986: Algorithm 644: a portable package for Bessel functions of a complex argument and nonnegative order. *ACM Trans. on Math. Soft.*, **12**, 265-273.

Brigham, E.O., 1974: *The Fast Fourier Transform.* Prentice-Hall, Englewood Cliffs, N.J., 252 pp.

Broutman, D., J.W. Rottman, and S.D. Eckermann, 2002: Maslov's method for stationary hydrostatic mountain waves. *Q. J. R. Meteorol. Soc.*, **128**, 1159-1171.

Broutman, D., J. W. Rottman, and S.D. Eckermann, 2003: A simplified Fourier method for non-hydrostatic mountain waves. *J. Atmos. Sci.*, **60**, 2686- 2696.

Broutman, D., and J.W. Rottman, 2004: A simplified Fourier method for computing the internal wavefield generated by an oscillating source in a horizontally moving, depth-dependent background. *Phys. Fluids*, **10**, 3682-3689.

Broutman, D., J. Ma, S.D. Eckermann, and J. Lindeman, 2006: Fourier-ray modeling of transient trapped lee waves. *Mon. Wea. Rev.,* **134***, 2849-2856.

Chandrasekhar, S., 1961: *Hydrodynamic and Hydromagnetic Stability.* Dover, New York, 654 pp.

Doyle, J.D., and Q. Jiang, 2006: Observations and numerical simulations of mountain waves in the presence of directional wind shear. *Q. J. R. Meteorol. Soc.*, **132,** 1877 – 1905.

Eckermann, S.D., D. Broutman, J. Ma, and J. Lindeman, 2006: Fourier-ray modeling of short-wavelength trapped lee waves observed in infrared satellite imagery near Jan Mayen. *Mon. Wea. Rev.*, **134**, 2830-2848.

Hastings, D. A., and P.K. Dunbar, 1998: Development and assessment of the Global Land One-km Base Elevation Digital Elevation Model (GLOBE). *International Society of Photogrammetry and Remote Sensing, Archives*, **32**, pp. 218-221.

Lighthill, J. 1978: *Waves in Fluids.* University Press, Cambridge, 504 pp.

Lipps, F., and R. Hemler, 1982: A scale analysis of deep moist convection and some related numerical calculations. *J. Atmos. Sc*i., **39**, 2192 – 2210.

Marks, C.J., and S.D. Eckermann, 1995: A three-dimensional nonhydrostatic ray-tracing model for gravity waves: Formulation and preliminary results for the middle atmosphere. *J. Atmos. Sci.*, **52**, 1959-1983.

Murphy, E. A., 2006: Comparison of vertical velocity from balloon rise rates to those obtained from the Smith – Fourier model. Presentation, October 2006, Hanscom AFB, MA. (unpublished)

Sinclair, P.C., and P.M. Kuhn, 1991: *Infrared Detection of High Altitude Clear Air Turbulence.* NOARL Technical Note 205, Naval Oceanographic and Atmospheric Research Laboratory, Monterey, CA, 49 pp.

Shutts, G.J., and A. Gadian, 1999: Numerical simulations of orographic gravity waves in flows which back with height. *Q. J. R. Meteorol. Soc.*, **125**, 2743-2765.

Smith, R.B., 2002: Chapter 5: Stratified flow over topography, pp. 119 – 159, in *Environmental Stratified Flows*, R. Grimshaw ed., Kluwer Acad. Publishers, Boston, 281 pp.

Smith, R.B., S. Skubis, J.D. Doyle, A.S. Broad, C. Kiemle, and H. Volkert, 2002: Mountain waves over Mont Blanc: Influence of a stagnant boundary layer. *J. Atmos. Sci.*, **59**, 2073 – 2092.

Sneddon, I.N., 1951: *Fourier Transforms*. Dover, New York, 542 pp.

Tanushev, N.M., J. Qian, and J.V. Ralston 2007: Mountain waves and Gaussian beams. *Multiscale Modeling and Simulation*, **6**, 688-709.

Wurtele, M.G., R.D. Sharman, and T.L. Keller, 1987: Analysis and simulation of a troposphere-stratosphere gravity wave model. Part 1. *J. Atmos. Sci.*, **44**, 3269-3281.

APPENDIX A. EIGENVALUE ANALYSIS OF THE VERTICAL STRUCTURE EQUATION

A Fourier-transformed steady-state elliptic partial differential equation for vertical velocity w (m/s) representing the vertical structure equation for a two dimensional system (x, z) is:

$$\frac{\partial^2 \hat{w}}{\partial z^2} + \left(l^2 - k^2\right)\hat{w} = 0 \tag{A1}$$

where $\hat{w}(k,z) = \hat{w}_r + i\hat{w}_i$, $(i = \sqrt{-1})$ is the complex vertical velocity transform or eigenvector:

$$\hat{w}(k,z) \equiv \frac{1}{\sqrt{2\pi}} \int_{-\infty}^{\infty} w(x,z)e^{ikx}dx \quad (\text{m}^2\ \text{s}^{-1}\ \text{rad}^{-1}) \tag{A2}$$

z is height or altitude (m), k^2 is the square of the one-dimensional horizontal wave number

$$k = \frac{2\pi}{L_x} \quad (rad\,/\,m) \tag{A3}$$

with L_x being the wavelength in the direction (x) of the horizontal wind velocity at 1 km height, and

$$l^2(z) = \frac{N^2}{U^2} - \frac{1}{U}\frac{\partial^2 U}{\partial z^2} \quad (rad\,/\,m^2) \tag{A4}$$

is the Scorer parameter. N is the Brunt-Vaisala frequency (s^{-1}) and U (m/s) is a horizontal wind speed. The hat symbol ^ designates those variables defined in the transform or wave number domain. The expression for the vertical dispersion relation or wave number is written as

$$m^2 = l^2 - k^2 \quad \left(rad\,/\,m^2\right)$$

The Scorer parameter l^2 is calculated using a vertical profile of temperature, pressure, relative humidity, and the horizontal wind speed and is defined as a real function. The eigenvalue k^2 is treated as complex. In the analysis, the eigenvector amplitude $\hat{w} = |\hat{w}|e^{i\phi}$ is described by its modulus $|\hat{w}|$ and phase angle ϕ where

$$|\hat{w}| \equiv \left(\hat{w}_r^2 + \hat{w}_i^2\right)^{\frac{1}{2}} \qquad (\text{m}^2/\text{radian sec})$$

$$\phi \equiv \tan^{-1}\left(\hat{w}_i / \hat{w}_r\right) \qquad (\text{radians})$$

The solution to (A1) as a boundary value problem is formulated here as a general complex matrix for a system of homogeneous linear equations:

$$A\vec{x} = b \tag{A5}$$

where $\vec{x}$ is the complex eigenvector, A is the operator matrix, which contains both the differential operator and dispersion relation, and b is the right-hand side term. Equation (A5) is solved for the eigenvector $\vec{x}$ by specifying the wavelength or eigenvalue k^2 repeatedly over a range of wavelengths. Each eigenvalue is associated with a column eigenvector with dimension equal to the matrix row dimension or number of vertical levels. The wavelength or eigenvalue which produces the maximum eigenvector modulus is selected as the "dominant" wavelength or eigenvalue mode.

For this boundary value problem, the boundary conditions are defined (following Shutts, 1997):

$$\hat{w}(k,0) = 1 \text{ at the lower boundary } z = 0 \tag{A6}$$

$$\frac{\partial \hat{w}(k,z_t)}{\partial z} + im\hat{w}(k,z_t) = 0 \text{ for the upper boundary } z = z_t \tag{A7}$$

This upper boundary condition is often referred to as the radiation boundary condition.

To formulate the linear operator matrix A, Eq. (A1) is approximated by the finite difference form:

$$\frac{\hat{w}_{j+1} - 2\hat{w}_j + \hat{w}_{j-1}}{\Delta z^2} + m_j^2 \hat{w}_j = 0 \tag{A8}$$

where Δz is the height differential separating evenly-spaced vertical levels. Equation (A8) possesses a second-order numerical error associated with truncation of the Taylor series. Similarly, the upper boundary condition, Eq. (A7) is approximated in forward finite difference form as:

$$\frac{\hat{w}_j - \hat{w}_{j-1}}{\Delta z} + im_j \hat{w}_j = 0 \tag{A9}$$

which has a first-order numerical error. Given the lower boundary condition, Eq. (A6), the matrix solution starts effectively with level $j = 2$. Grouping terms, level 2 is written:

$$\frac{\hat{w}_3 - 2\hat{w}_2}{\Delta z^2} + m_2^2 \hat{w}_2 = 0 \tag{A10}$$

From levels $j = 3$ through levels $j = n - 1$, where n is the top level, Eq. (A8) can be expressed as:

$$\frac{\hat{w}_{j+1} + \hat{w}_{j-1}}{\Delta z^2} + \left(m_j^2 - \frac{2}{\Delta z^2} \right) \hat{w}_j = 0 \tag{A11}$$

For level $j = n$, using the upper boundary condition (A9):

$$\left(im_j + \frac{1}{\Delta z} \right) \hat{w}_j - \frac{\hat{w}_{j-1}}{\Delta z} = 0 \tag{A12}$$

The operator matrix A is constructed to solve for the column eigenvector $\hat{w}$ from levels $j = 2$ through levels $j = n$. This yields a tridiagonal matrix of order $(n-1) \times (n-1)$. The problem can be solved numerically for $\bar{x}$ using a subroutine solver, given the general tridiagonal matrix A and right-hand side column vector b, or using a relatively simple non-iterative algorithm akin to Gaussian elimination for solving second order ordinary differential equations as a two point boundary value problem (Lindzen and Kuo, 1969). Both methods yield identical results for the dominant mode. For the calculations described below, the dominant eigenmode was selected as the wavenumber that has the maximum eigenfunction modulus over of a range of 200 wavenumbers ranging in wavelength from 0.25 km to 50 km.

An advantage of the eigenanalysis relative to Fourier wave methods appears to be that it allows relatively high-resolution continuous vertical profiles of static stability and wind speed or shear (Scorer parameter) to serve as the basic state for determining a vertical profile solution using the matrix inversion method required by vertical discretization. The eigenanalysis also permits quick determination of the dominant wavelength modes associated with the basic state and their vertical structure. A disadvantage is there is no provision for direct inclusion of terrain in the lower boundary condition in this approach.

A.1 Sample calculation

The eigenvalue calculations are sensitive to the specification of the Scorer parameter, especially to whether the second term in the right hand side of Eq. (A4) -- the wind curvature term --is retained, but appear less sensitive to the number of model levels or matrix dimension. The Scorer parameter is calculated following the numerical procedures described by Shutts (1997) using a height differential $\Delta z = 100$ meters and the horizontal wind speed component parallel to the wind direction at $z = 1$ km. This altitude corresponds, presumably, with the mountain's ridge top altitude. Test calculations (not shown) were performed for selected horizontal wavelengths and varying numbers of matrix levels using a sample thermosonde profile. The results for individual modes exhibited sensitivity to the inclusion of the second term in the Scorer parameter (the shear derivative) in the lower 10 km. When the matrix dimensions were increased from 200 to 300 levels, little change was observed in the eigenfunction behavior.
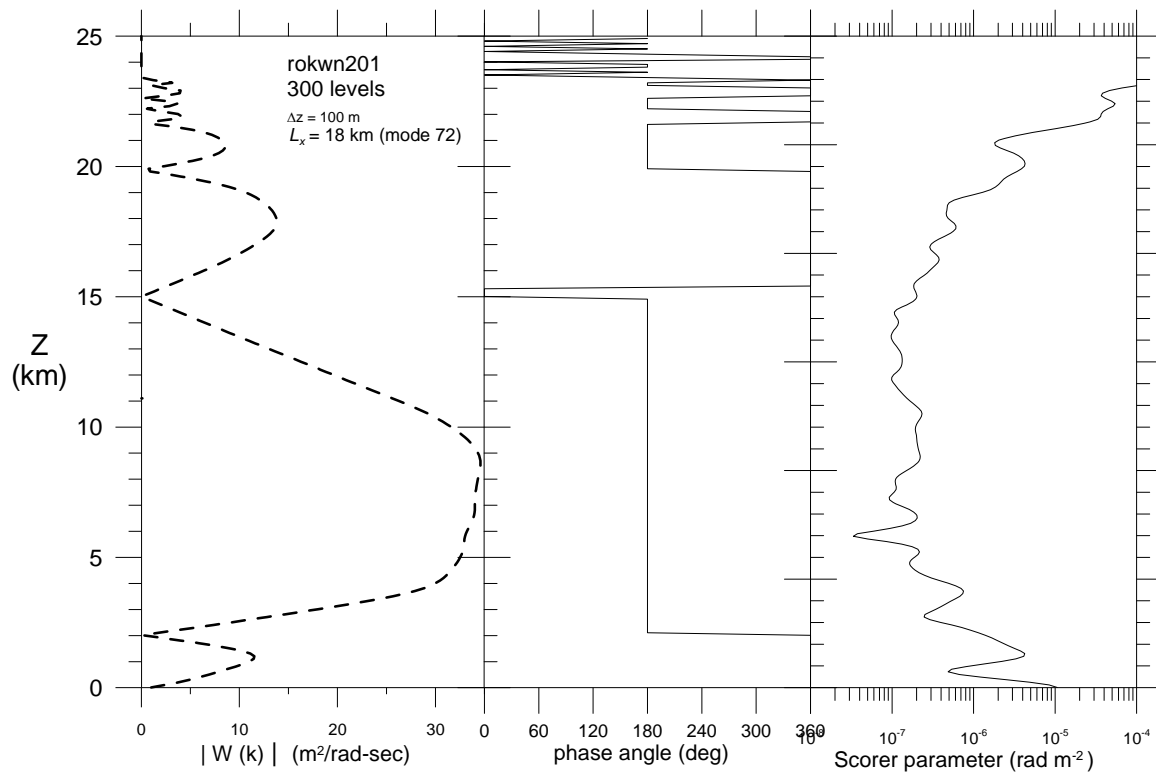

Figure A1: Eigenvector profiles for the dominant mode (# 72, L_x = 18 km) and the Scorer parameter profile, without the second term on the right hand side of Eq. (A4).

The features of the dominant mode for a sample rawinsonde profile (rokwn201), at a wavelength of 18 km (mode 72), are plotted as a function of altitude in Figure A1. These include modulus, phase, and the Scorer parameter with the second term involving the second derivative omitted. The modulus peaks around 8 to 9 km with a phase angle of 180 degrees. This implies a zero or negligible imaginary component for the eigenvector over the region of its maximum amplitude.

Behaviors of the dominant modes for 18 rawinsonde profiles as a function of wavelength are illustrated in figure A2. The peak moduli for the dominant modes were determined objectively while the dominant mode tops were determined by inspection of moduli contours plotted as a function of wave number and altitude. These results imply the depth of the dominant mode is inversely proportional to the wavenumber magnitude, or proportional to the wavelength. Shallow dominant modes are associated with shorter wavelengths while the taller or deeper dominant modes are associated with longer wavelengths. In addition, the logarithm of the wavelength of the dominant modes is somewhat proportional to the logarithm of the eigenmode moduli.
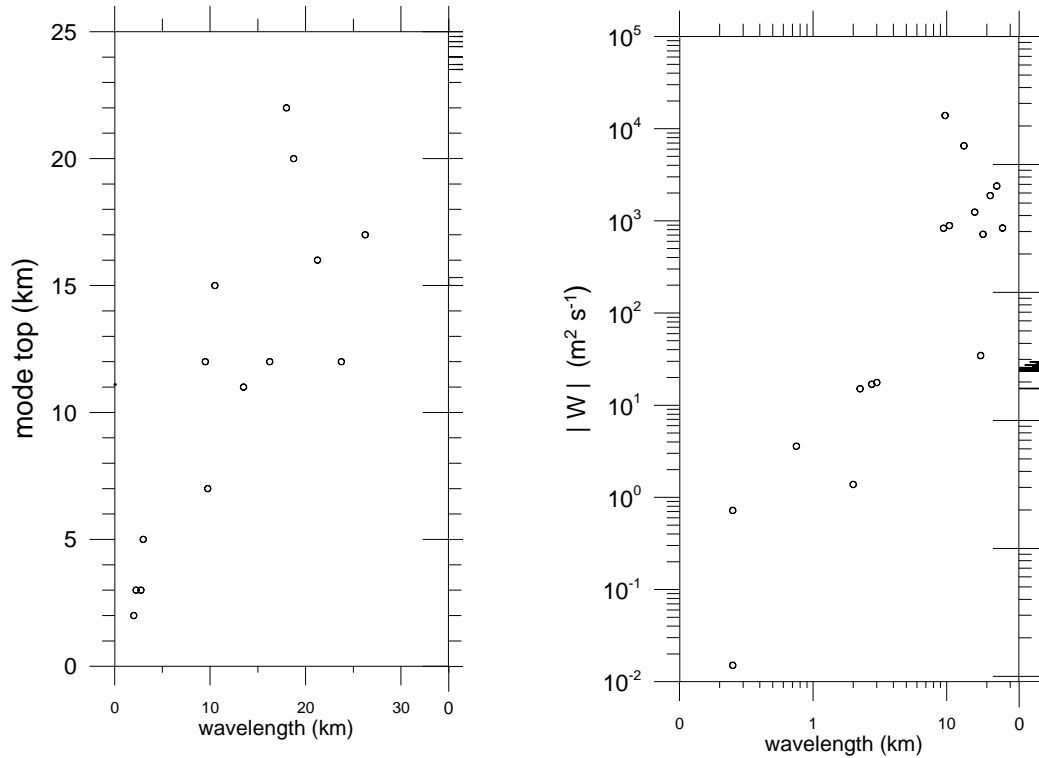

Figure A2: Dominant eigenvector mode tops (km) and peak moduli ($m^2 s^{-1}$) as a function of wavelength (km). Each open circle represents the dominant eigenmode for a single Scorer parameter profile.

References

Lindzen, R.S., and H.L. Kuo, 1969: A reliable method for the numerical integration of a large class of ordinary and partial differential equations. *Mon. Wea. Rev.*, **97**, 732-734.

Shutts, G., 1997: Operational lee wave forecasting. *Meteorol. Appl.*, **4**, 23-35.

APPENDIX B. REPRESENTATIONS OF THE AIRY FUNCTION

Airy function: $Ai(z) = \dfrac{1}{\pi}\displaystyle\int_0^\infty \cos\left(\tfrac{1}{3}t^3 + zt\right)dt$ (integral representation)

1. Using ascending series for small $|z|$:

$$Ai(z) = c_1 f(z) - c_2 g(z) \qquad c_1 = 0.355028053887817 \quad c_2 = 0.258819403792807$$

$$f(z) = \sum_0^\infty \frac{3^k \cdot z^{3k}}{(3k)!}\frac{\Gamma(1/3+k)}{\Gamma(1/3)} \quad ; \quad g(z) = \sum_0^\infty \frac{3^k z^{3k+1}}{(3k+1)!}\frac{\Gamma(2/3+k)}{\Gamma(2/3)}$$

$k = 1, 2, 3, \ldots \qquad r! = \Gamma(r+1) \qquad z$ can be real or complex: r is real

2. Using asymptotic expansion for large $|z|$:

$$Ai(z) \sim \frac{1}{2}\pi^{-\frac{1}{2}} z^{-\frac{1}{4}} e^{-\zeta} \sum_0^\infty (-1)^k c_k \zeta^{-k} \text{ where}$$

$$\zeta = \frac{2}{3} z^{\frac{3}{2}} \quad ; \quad c_k = \frac{\Gamma\left(3k+\frac{1}{2}\right)}{54^k k!\,\Gamma\left(k+\frac{1}{2}\right)}$$

$$Ai(-z) \sim \pi^{-\frac{1}{2}} z^{-\frac{1}{4}}\left[\sin\left(\zeta+\frac{\pi}{4}\right)\sum_0^\infty (-1)^k c_{2k}\zeta^{-2k} - \cos\left(\zeta+\frac{\pi}{4}\right)\sum_0^\infty (-1)^k c_{2k+1}\zeta^{-2k-1}\right]$$

3. Auxiliary functions for large negative real z:

$$Ai(-z) = z^{-\frac{1}{4}}\left[f_1(\zeta)\cos\zeta + f_2(\zeta)\sin\zeta\right] \quad \text{(see p. 477 of Abramowitz and Stegun, 1972)}$$

4. Auxiliary functions for large positive real $z = x + 0i$:

$$Ai(z) = \frac{1}{2}z^{-\frac{1}{4}} e^{-\zeta} f(-\zeta) \quad \text{(see p. 475 of Abramowitz and Stegun, 1972)}$$
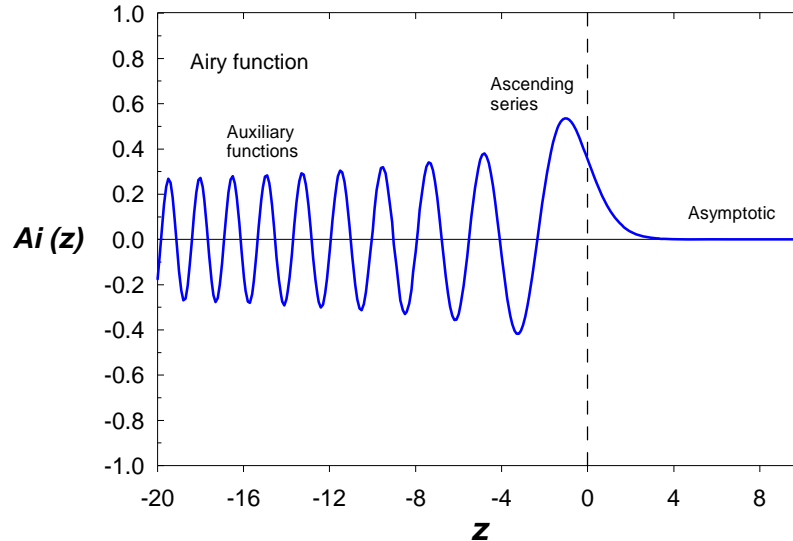

Figure B1. Airy function along the real axis

Fast parameterization of Airy function where z is real:

1. $z > 1.0$: use auxiliary function for large positive z (item 4.)
2. $-0.5 < z < 1.0$: use polynomial fit
3. $-7.0 < z < -0.5$: use Lighthill (1978) approximation for substantial negative z

$$Ai(z) \sim \pi^{-\frac{1}{2}} z^{-\frac{1}{4}} \cos\left(\tfrac{2}{3} z^{\frac{3}{2}} - \tfrac{1}{4}\pi\right)$$

4. $z < -7.0$ use auxiliary function for large negative z (item 3.)

References

Abramowitz, M.. and I. Stegun, 1972: *Handbook of Mathematical Functions*, Dover, New York, 1046 pp.

Amos, D.E., 1986: Algorithm 644: a portable package for Bessel functions of a complex argument and nonnegative order. *ACM Trans. on Math. Soft.*, **12**, 265-273.

Lighthill, J. 1978: *Waves in Fluids*. University Press, Cambridge, 504 pp.

Miller, J.C.P., 1946: *"The Airy Integral"* in *Mathematical Tables, Volume B,* British Assoc. for the Advancement of Science, University Press, Cambridge, 48 pp.

Woodward, P.M., A.M. Woodward, R. Hensman, H. Davies, and N. Gamble, 1946: Four-figure tables of the Airy function in the complex plane. *Phil. Mag.*, **37**, 236-261
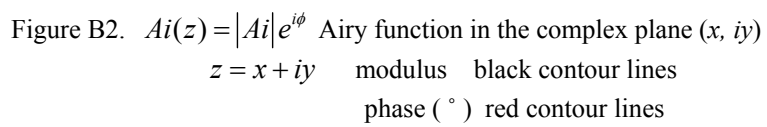
Figure B2. $Ai(z) = |Ai|e^{i\phi}$ Airy function in the complex plane (x, iy)
$z = x + iy$ modulus black contour lines
phase (˚) red contour lines

ACM machine algorithm (Amos, 1986) $Ai(x+iy) = |Ai|e^{i\phi}$

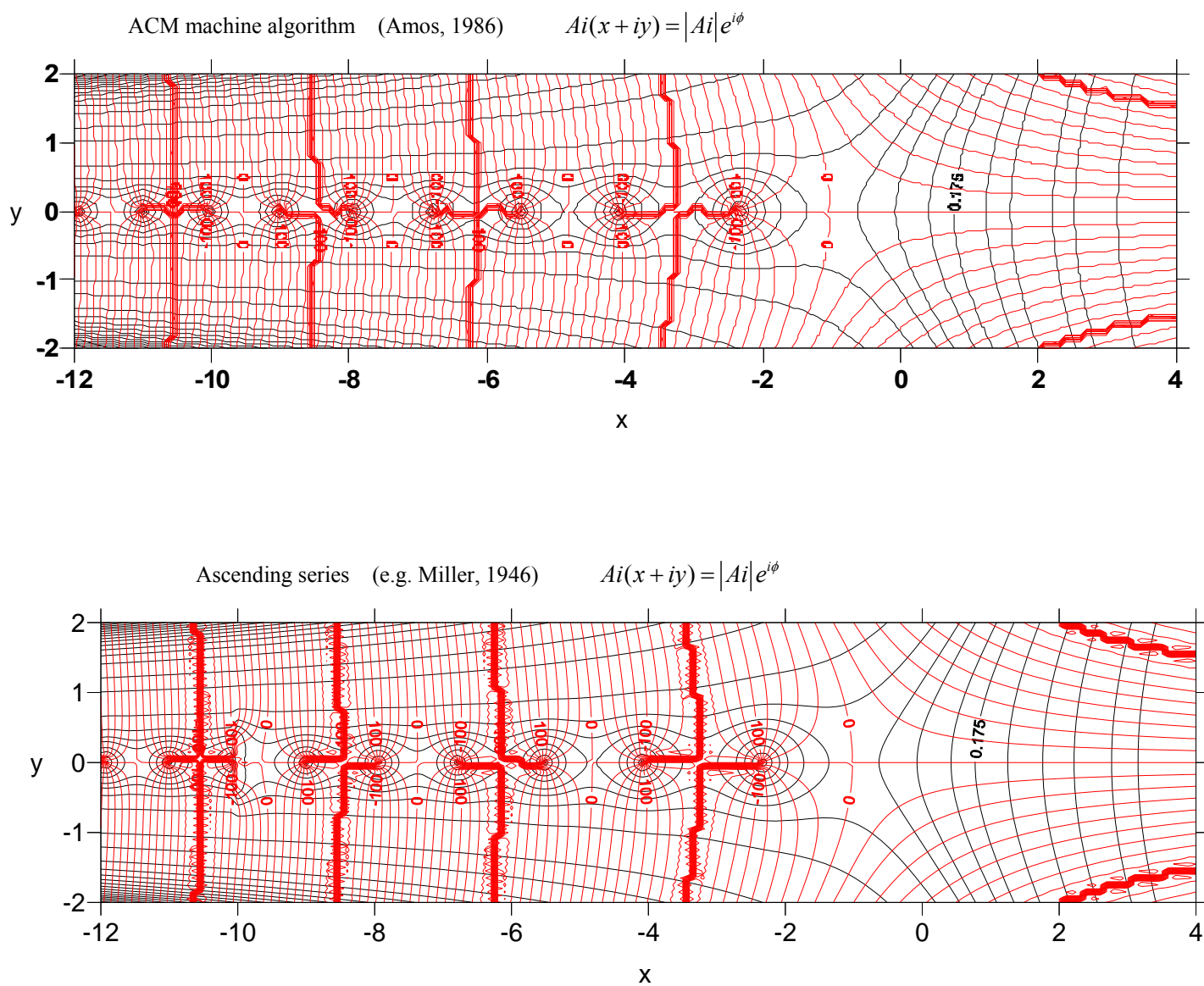Ascending series (e.g. Miller, 1946) $Ai(x+iy) = |Ai|e^{i\phi}$

Figure B3. Comparison of machine and series solutions for the Airy function in the complex plane (x, iy). Contour analysis follows the same format as figure B2.